Cell Reports

Article

Intrinsic antiviral immunity of barrier cells revealed by an iPSC-derived blood-brain barrier cellular model

Graphical abstract

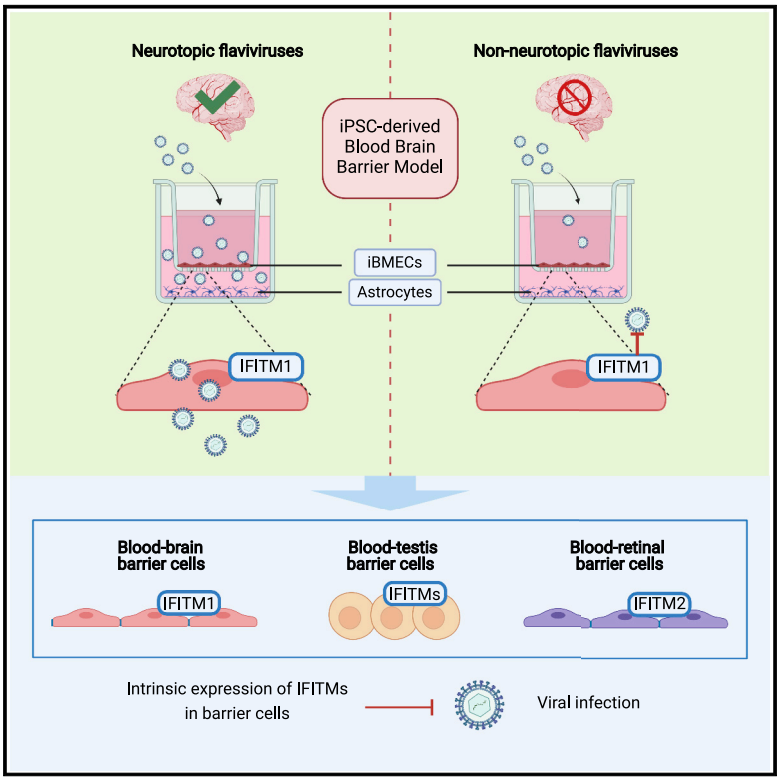

Highlights

- iPSC-derived BBB cells recapitulate the *in vivo* phenotype of neuroinvasive viruses
- An iBMEC/astrocyte coculture exhibits high TEER and models viral neuroinvasion
- Constitutive expression of IFITM1 selectively inhibits non-neurotropic flaviviruses
- Intrinsic expression of IFITMs contributes to broad barrier-based virus restriction

Authors

Yichen Cheng, Angelica Medina, Zhenlan Yao, ..., Margo A. Brinton, Melody M.H. Li, Hengli Tang

Correspondence

tang@bio.fsu.edu

In brief

Using a stem cell-derived cellular model and a panel of human pathogenic viruses, Cheng et al. show a mechanism by which some viruses can penetrate the blood-brain barrier and cause diseases in the central nervous system.

Cheng et al., 2022, Cell Reports *39*, 110885
May 31, 2022
https://doi.org/10.1016/j.celrep.2022.110885

CellPress

Cell Reports

CellPress
OPEN ACCESS

Article

Intrinsic antiviral immunity of barrier cells revealed by an iPSC-derived blood-brain barrier cellular model

Yichen Cheng,[1,6] Angelica Medina,[1,6] Zhenlan Yao,[2] Mausumi Basu,[3] Janhavi P. Natekar,[3] Jianshe Lang,[1] Egan Sanchez,[1] Mezindia B. Nkembo,[1] Chongchong Xu,[4] Xuyu Qian,[5] Phuong T.T. Nguyen,[5] Zhexing Wen,[4] Hongjun Song,[5] Guo-Li Ming,[5] Mukesh Kumar,[3] Margo A. Brinton,[3] Melody M.H. Li,[2] and Hengli Tang[1,6,7,*]

[1]Department of Biological Science, Florida State University, Tallahassee, FL, USA
[2]Department of Microbiology, Immunology, and Molecular Genetics, University of California, Los Angeles, Los Angeles, CA, USA
[3]Department of Biology, Georgia State University, Atlanta, GA, USA
[4]Department of Psychiatry and Behavioral Sciences, Emory University School of Medicine, Atlanta, GA, USA
[5]Department of Neuroscience, Perelman School of Medicine, University of Pennsylvania, Philadelphia, PA, USA
[6]These authors contributed equally
[7]Lead contact
*Correspondence: tang@bio.fsu.edu
https://doi.org/10.1016/j.celrep.2022.110885

SUMMARY

Physiological blood-tissue barriers play a critical role in separating the circulation from immune-privileged sites and denying access to blood-borne viruses. The mechanism of virus restriction by these barriers is poorly understood. We utilize induced pluripotent stem cell (iPSC)-derived human brain microvascular endothelial cells (iBMECs) to study virus-blood-brain barrier (BBB) interactions. These iPSC-derived cells faithfully recapitulate a striking difference in *in vivo* neuroinvasion by two alphavirus isolates and are selectively permissive to neurotropic flaviviruses. A model of cocultured iBMECs and astrocytes exhibits high transendothelial electrical resistance and blocks non-neurotropic flaviviruses from getting across the barrier. We find that iBMECs constitutively express an interferon-induced gene, IFITM1, which preferentially restricts the replication of non-neurotropic flaviviruses. Barrier cells from blood-testis and blood-retinal barriers also constitutively express IFITMs that contribute to the viral resistance. Our application of a renewable human iPSC-based model for studying virus-BBB interactions reveals that intrinsic immunity at the barriers contributes to virus exclusion.

INTRODUCTION

Physiological barriers are an integral part of host defense against invading pathogens. In addition to external barriers such as skin and mucosal secretions, internal blood-tissue barriers function to separate circulation compartment from the immune-privileged organs, such as brain, eye, and testis. Although these barriers have their evolutionary roots in the protection of these vital structures from unintended damage by inflammatory responses, they also function to separate viremia from tissues and restrict access by blood-borne pathogens. The blood-brain barrier (BBB) consists of brain microvascular endothelial cells (BMECs) supported by astrocytes and pericytes (Abbott et al., 2006). The BMECs line the blood vessels that border brain parenchyma and form tight junctions (TJ). The TJ proteins, along with the efflux transporter P-glycoprotein on the surface of BMECs, help to repel circulating molecules and pathogens, whereas high expression of the glucose transporter protein type 1 (GLUT1) allows transport of glucose into the brain to meet energy needs (Daneman and Prat, 2015). Similarly, Sertoli cells (SerCs), retinal pigment epithelial (RPE) cells, and retinal microvascular endothelial cells (RMECs or RvECs) function at the blood-testis barrier (BTB), the inner blood-retinal barrier (BRB), and the outer BRB, respectively to regulate material exchange and protect the testes and eyes (Campbell and Humphries, 2012; Mruk and Cheng, 2015).

While the barriers are highly effective in denying entry by most viruses, some have evolved the ability to breach them. For example, neuroinvasive viruses can access the central nervous system (CNS) and cause neurological diseases. Why certain viruses are neuroinvasive whereas others are not is poorly understood. Although non-BBB routes of CNS invasion such as the retrograde transport of herpes simplex virus infecting peripheral neurons are well recognized, the majority of the neuroinvasion mechanisms involve an interaction between the virus and the BBB (Cain et al., 2019). These mechanisms include direct infection of the endothelial cells, disruption of the barrier, and transport via surface absorption to transmigrating immune cells. Both *in vivo* and *in vitro* models have been developed to study virus-BBB interactions. Animal models can provide a definitive

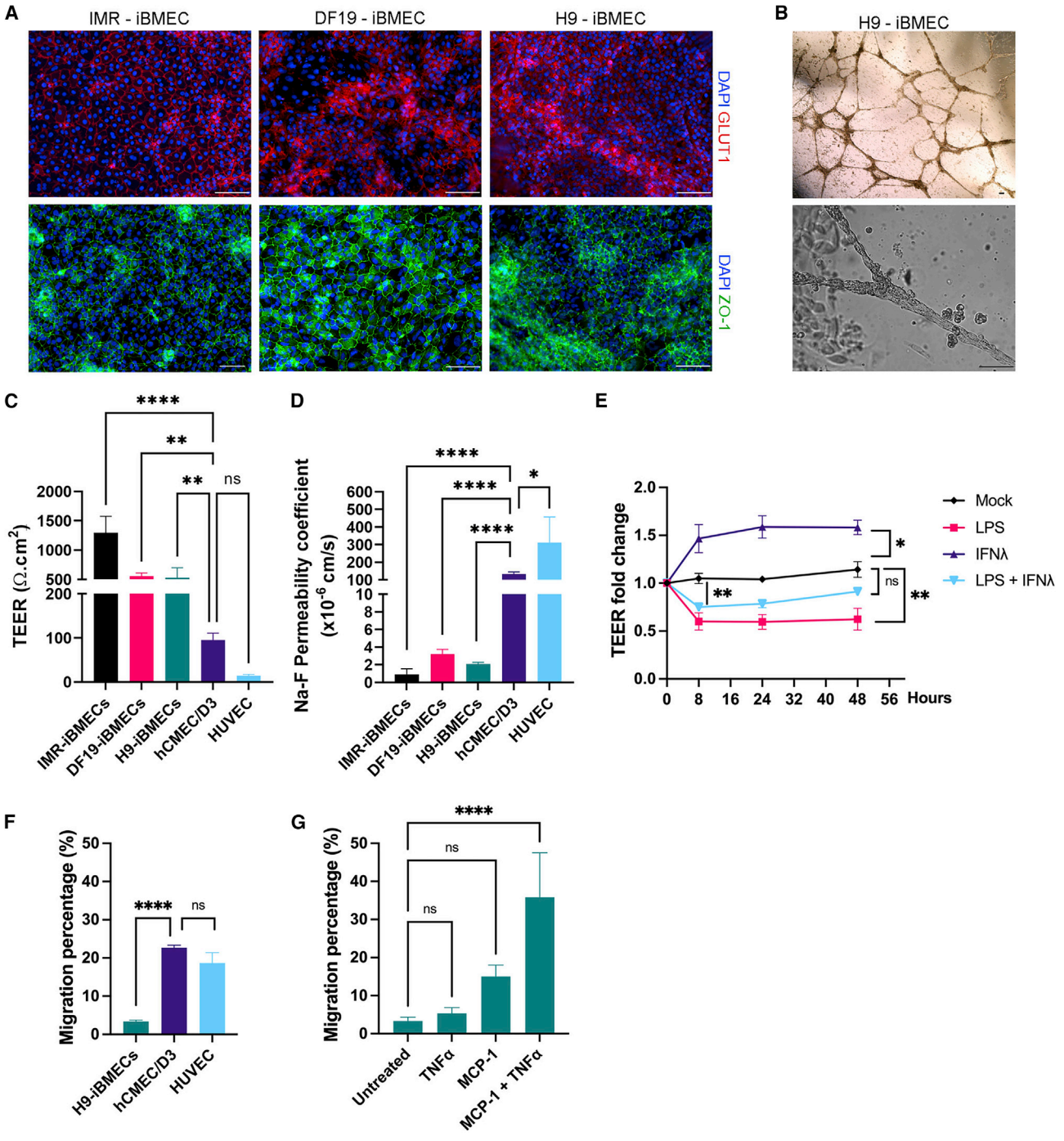

Figure 1. iBMECs exhibit barrier characteristics and respond to inflammation and IFN signaling

(A) Expression of cell-surface markers on iBMECs. Scale bars, 100 μm.

(B) Representative images of vascular tubes formed by the iBMECs. Scale bars, 100 μm.

(C) TEER of cell monolayers on transwells. Measurements were taken 48–72 h after cell seeding.

(D) Sodium fluorescein (Na-F) permeability of iBMECs. Measurements were taken 48–72 h after cell seeding.

(E) Barrier response to LPS (100 ng/mL) and IFN (100 ng/mL). For the LPS and IFN double treatment, LPS was added 48 h after seeding (0 h time point) followed by addition of IFN-λ1 8 h later. TEER measurements were taken at the indicated times. A two-way ANOVA was performed.

(legend continued on next page)

answer as to whether a virus is neuroinvasive *in vivo*, although they are less amenable to the dissection of molecular mechanisms. For example, neurovirulence determinants and related pathways for neurotropic alphaviruses have been well studied using the mouse model (Atkins and Sheahan, 2016; Hollidge et al., 2021; Kendra et al., 2017). *In vitro* models include primary BMECs, cell lines derived from BMECs, and differentiated cells derived from pluripotent stem cells (PSCs). The BMECs induced from PSCs (iBMECs) (Lippmann et al., 2012) are a particularly promising model, as they overcome both the limited source of primary human cells and the low transendothelial electrical resistance (TEER) of the cell lines. The differentiation protocol generally utilizes codifferentiation with neural cells followed by specific selection for endothelial cells (Lippmann et al., 2012). Additional improvements such as addition of retinoic acid or overexpression of endothelial transcription factors enhanced endothelium maturation (Lippmann et al., 2014; Lu et al., 2021; Qian et al., 2017). The iBMEC model has been used to study the CNS permeability of therapeutics and viral invasion (Alimonti et al., 2018; Lippmann et al., 2020).

The genus *Flavivirus* includes many vector-borne RNA viruses that are pathogenic in humans and present a significant threat to global health. Despite similarities in genome structure and transmission vectors, individual flaviviruses differ significantly in their tissue tropism and disease outcomes. A salient feature of a subgroup of these viruses, including Zika virus (ZIKV), West Nile virus (WNV), and Japanese encephalitis virus (JEV), is their ability to invade the brain and cause CNS diseases. In contrast, yellow fever virus-17D (YFV-17D) and dengue virus (DENV) are not known to invade CNS in immune-competent hosts. Given these similarities and differences, the flaviviruses are well suited for studying the molecular mechanisms underlying viral neuroinvasiveness.

Induction of interferon (IFN) response following infection is an integral part of the innate immunity. IFN activates IFN-stimulated genes (ISGs), which are a large group of proteins normally only expressed upon IFN signaling. However, certain ISGs can also be expressed constitutively in an IFN-independent manner. Indeed, constitutive expression of a subset of antiviral ISGs by PSCs (Wu et al., 2012, 2018) protects these important cells from viral infection (Wu et al., 2018). Individual antiviral ISGs deploy distinct antiviral mechanisms, and, collectively, ISGs can restrict infection by many viruses (Schoggins et al., 2011). The number of viruses targeted by a particular ISG varies, but even the ISGs with broad-spectrum activities, such as the IFN-induced transmembrane protein (IFITM) family, are only effective against a limited number of viruses (Brass et al., 2009). The contribution of intrinsically expressed antiviral ISGs in barrier cells to the blockage of a virus infecting the barrier has not been explored.

Here we report the application of human iBMECs to a mechanistic study of virus-BBB interaction. We demonstrate that the iBMECs effectively model the neuroinvasiveness of both alphaviruses and flaviviruses. We further discover that the antiviral ISG IFITM1 is constitutively expressed by iBMECs, and its function toward different flaviviruses contributes to the selective restriction of these viruses. In addition, SerCs and RMECs also intrinsically express IFITM proteins that exhibit antiviral function. Our study suggests that cell-autonomous antiviral immunity represents a broad mechanism for controlling viral invasion of physiological blood-tissue barriers.

RESULTS

Human PSC-derived iBMECs exhibit barrier characteristics and respond to inflammation and IFN signaling

We derived iBMECs from three human PSC lines including two induced PSC (iPSC) lines, IMR90-4 (IMR) and DF19-9-11T (DF19), and an embryonic stem cell line, H9, using a protocol adapted from the literature (Lippmann et al., 2012, 2014; Neal et al., 2019) (Figure S1A). The iBMECs expressed endothelial markers CD31 and VE-cadherin, TJ proteins Claudin-5 and ZO-1, and transporter proteins GLUT1 and P-glycoprotein (Figures 1A and S1B–S1D). In addition, these cells formed vascular tube-like structures upon treatment with vascular endothelial growth factor (Figure 1B). To further evaluate the barrier function of the iBMECs, we measured their TEER values and permeability to sodium fluorescein (Na-F). The monolayers formed by iBMECs exhibited higher TEER values and were much less permeable compared with those formed by human umbilical vein endothelial cells (HUVECs) or the BMEC cell line hCMEC/D3 (Weksler et al., 2005) (Figures 1C and 1D). The IMR-iBMEC monolayer consistently produced the highest TEER values and the lowest Na-F permeability. In addition, we observed that rhodamine 123 accumulated more efficiently in the iBMECs in the presence of cyclosporin A treatment, indicating the presence of a functional P-glycoprotein efflux transporter (Figure S1E).

The tightness of the BBB is regulated by immune and inflammatory signaling molecules such as bacterial lipopolysaccharides (LPSs) and type III IFN (Daniels et al., 2014, 2017; Eckman et al., 1958; Kraus et al., 2004; Lazear et al., 2015; Salimi et al., 2020). We determined whether the iBMEC monolayer can respond to these signals. LPS treatment compromised the barrier tightness, and this effect was reversed by type III IFN (Figure 1E). In a monocyte migration assay, the basal migration rate of the monocytic THP-1 cells through the iBMEC monolayer was lower when compared with that through the hCMEC/D3 or the HUVEC monolayer (Figure 1F). Treating the cells with monocyte chemoattractant protein-1 (MCP-1) and inflammatory cytokine tumor necrosis factor α (TNF-α) resulted in increased monocyte migration without compromising barrier integrity (Figures 1G and S1F–S1G). Together, these results demonstrate

(F and G) Monocyte migration rate through (F) the cell monolayers and (G) iBMECs in response to stimuli. THP-1 cells were added to the apical chamber of the transwell 48 h after seeding of iBMECs. In (G), MCP-1 was added to the basolateral chamber and TNF-α to the apical chamber. Quantification of THP-1 cells that reached the basolateral chamber was performed 18 h later.

Values shown as mean ± SD from a minimum of three biological replicates. A one-way ANOVA was performed unless otherwise indicated. Throughout this study, asterisks indicate statistically significant differences (*$p \leq 0.05$; **$p \leq 0.01$; ***$p \leq 0.001$; ****$p \leq 0.0001$; ns, no significance).

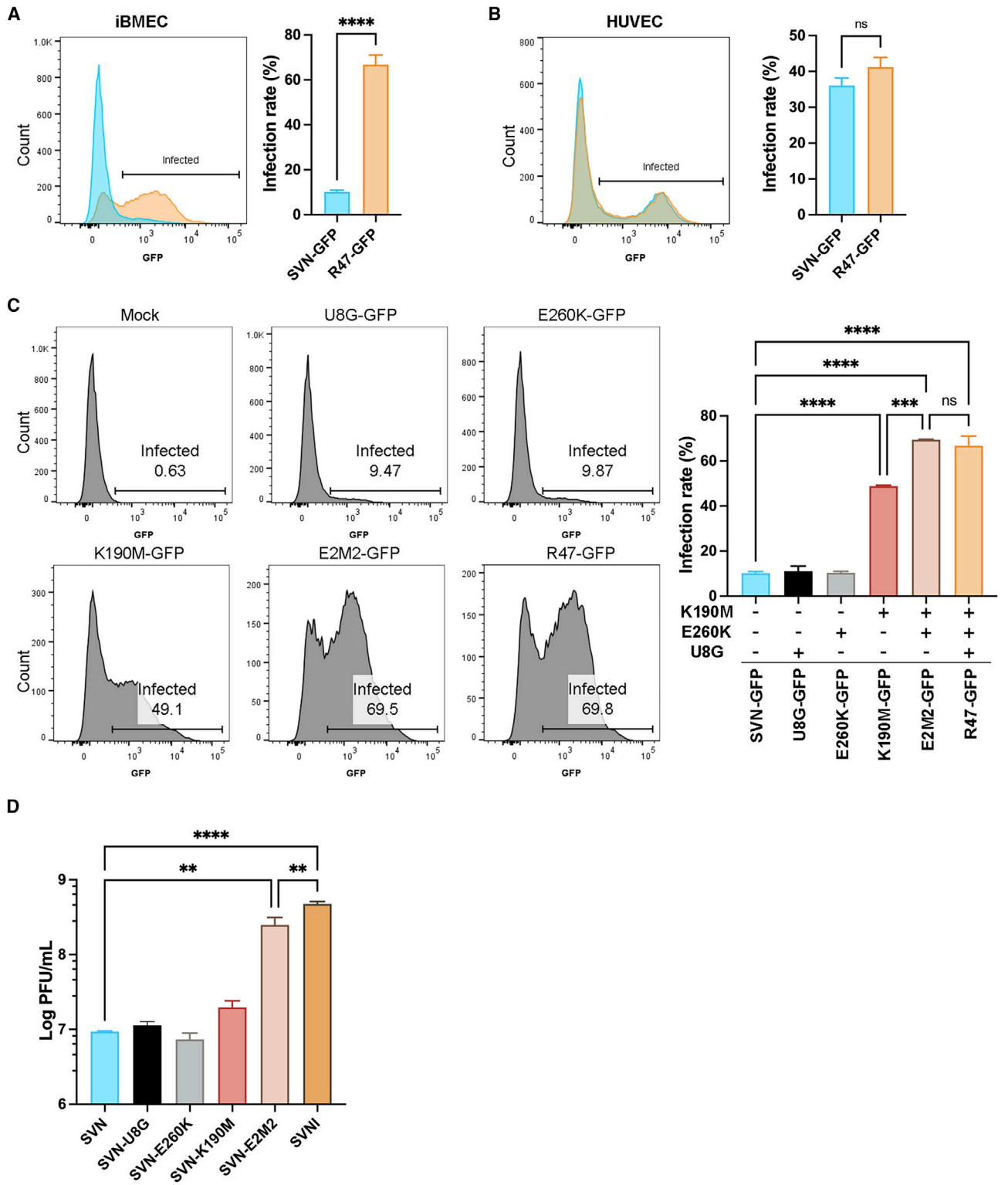

Figure 2. The iBMECs recapitulate *in vivo* neuroinvasiveness of alphavirus

(A and B) Fluorescence-activated cell sorting (FACS) profiles and quantification of (A) iBMECs and (B) HUVECs after infection with alphaviruses. Cells were collected for flow cytometry 24 h post infection (hpi). Multiplicity of infection (MOI) = 3.

(legend continued on next page)

that the iBMEC barrier model recapitulates *in vivo* characteristics of the BBB structure under physiological conditions.

The iBMECs recapitulate *in vivo* neuroinvasiveness of alphavirus

To test the suitability of the iBMECs to model neuroinvasiveness of viruses, we selected a pair of closely related Sindbis virus (SINV) strains, SVN and SVNI, with distinct neuroinvasive characteristics (Dubuisson et al., 1997) (Figure S2A). SVN is a neurovirulent but non-neuroinvasive strain that normally replicates in the periphery without lethality in weanling mice while SVNI is a neurovirulent and neuroinvasive strain that infects the CNS and causes lethal encephalitis even when inoculated peripherally (Lustig et al., 1992). A subsequent study mapped the neuroinvasion determinants to three mutations: a uracil to guanine change at position 8 (U8G) in the viral 5′ non-coding region and two amino acid changes (K190M, E260K) in the E2 glycoprotein (Dubuisson et al., 1997). We found that similar to what was observed in mice, the SVN mutant carrying G8, M190, and K260, named R47 (Figure S2A), is able to efficiently infect iBMECs while SVN cannot (Figure 2A). On the contrary, both viruses can efficiently infect HUVECs (Figure 2B) and a human glioblastoma cell line, SNB-19 (Figure S2B). We then analyzed the single mutations and a double mutant of E2. The two E2 mutations were sufficient to rescue SVN replication and production in iBMECs to levels similar to those of R47 and SVNI (Figures 2C and 2D). Interestingly, K190M alone is able to significantly rescue viral replication but not viral production while U8G or E260K alone has no effects on viral replication and production. Taken together, these results clearly establish the iBMECs as an excellent model for recapitulating and characterizing *in vivo* virus-BBB interactions.

Differential infection of iBMECs by neurotropic versus non-neurotropic flaviviruses

We next exposed the iBMECs to a panel of neuroinvasive and non-neuroinvasive flaviviruses that included an Asian and an African strain of ZIKV, four isolates of DENV representing each of the serotypes, three strains of WNV, and one strain each of YFV, JEV, and Usutu virus (USUV). While ZIKV could efficiently infect iBMECs, DENV infection was below detection level (Figures 3A and 3B). The iBMECs from three stem cell lines all exhibited the differential infection phenotype (Figures 3A and S3A). None of the four DENV isolates tested could productively infect these cells (Figures S3A and S3B). Of the three strains of WNV tested, the two neuroinvasive strains, NY99 and Eg101 (Beasley et al., 2002; Kumar et al., 2016), were able to efficiently infect iBMECs and produce high titers of virus. The non-neuroinvasive strain, MAD78 (Beasley et al., 2002), on the other hand, produced virus titers that were approximately 100-fold lower (Figures 3C, 3F, and S3C). Additional neuroinvasive flaviviruses, JEV and USUV (Cle et al., 2020; Hsieh et al., 2019), productively infected the iBMECs (Figures 3F and S3C) while YFV-17D did not efficiently infect these cells (Figures 3D, 3E, and S3D). DENV-2 and YFV-17D were nevertheless capable of infecting Huh7.5 cells, a highly permissive cell line for flavivirus infection (Figures 3D and 3E), suggesting a selective block of infection of these non-neuroinvasive viruses by the iBMECs.

The iBMEC barrier blocks transendothelial infection of CNS cells by non-neurotropic flaviviruses

BBB integrity is regulated by astrocytes and other CNS cells besides the endothelial layer. While the effect of coculturing iBMECs with human neural progenitor cells (hNPCs) or forebrain organoids were variable and limited in magnitude in terms of TEER increase (Figures S4A–S4C), the coculture of IMR-iBMECs with astrocytes resulted in a large increase of the TEER value to approximately 5,000 $\Omega.cm^2$ (Figure S4D). Interestingly, the response to astrocytes was limited to progenies from IMR (Figure S4D), suggesting that variations between the stem cell lines can affect the ability of the iBMECs to respond to brain cells. Given these results, we selected the IMR-iBMECs/astrocyte coculture model to test the ability of the barrier to block viral infection of CNS cells. We inoculated the viruses into the upper chamber of the transwell with or without an iBMEC monolayer and then assessed infection of the astrocytes in the lower chamber. The presence of the iBMEC monolayer effectively blocked the infection of the astrocytes by DENV-2 and YFV-17D whereas ZIKV efficiently infected the astrocytes with or without the monolayer barrier (Figure 4A). The ability of a virus to be detected in the lower chamber in this model was not correlated with barrier disruption because neither ZIKV nor YFV-17D had any effect on the TEER values (Figure 4B). Although DENV-2 induced a reduction in TEER, this decrease was not sufficient to allow the virus, even when added again at the time after the decrease, to reach the lower chamber of the transwell (Figure 4C). JEV and USUV efficiently accessed and infected the astrocytes in this model (Figures 4D and S4E). Of the three WNV strains tested, NY99 and Eg101 were able to infect the astrocytes while MAD78 inefficiently accessed the lower chamber and infected few astrocytes (Figures 4C and S4E). Overall, WNV did not affect the TEER values (Figure 4E), consistent with results in primary BMECs (Verma et al., 2009). JEV and USUV both compromised the barrier and replicated efficiently in the astrocytes (Figures 4D, 4F, and S4E). Finally, when forebrain organoids were placed at the lower chamber to represent the CNS cells, a similar differential infection by ZIKV, DENV-2, and YFV-17D was observed (Figure 4F).

The iBMECs intrinsically express IFITM1 that restricts DENV but not ZIKV infection

Our results so far indicate that the ability to infect iBMECs is a major correlate of neuroinvasiveness of the viruses tested. We first determined whether the restricting mechanism for DENV is cell autonomous or conferred by signaling from secreted factors such as type III IFN, which inhibits ZIKV infection of placental and vaginal cells (Bayer et al., 2016; Caine et al., 2019). To address

(C) FACS profile and quantification of iBMECs after infection with SVN mutants. Cells were collected at 24 hpi. MOI = 3.
(D) Virus titer of supernatants collected from iBMECs infected with alphaviruses. Supernatants were collected 24 hpi for titration quantified as plaque-forming units (PFU). MOI = 3.
Values are shown as mean ± SD from two independent infection experiments.

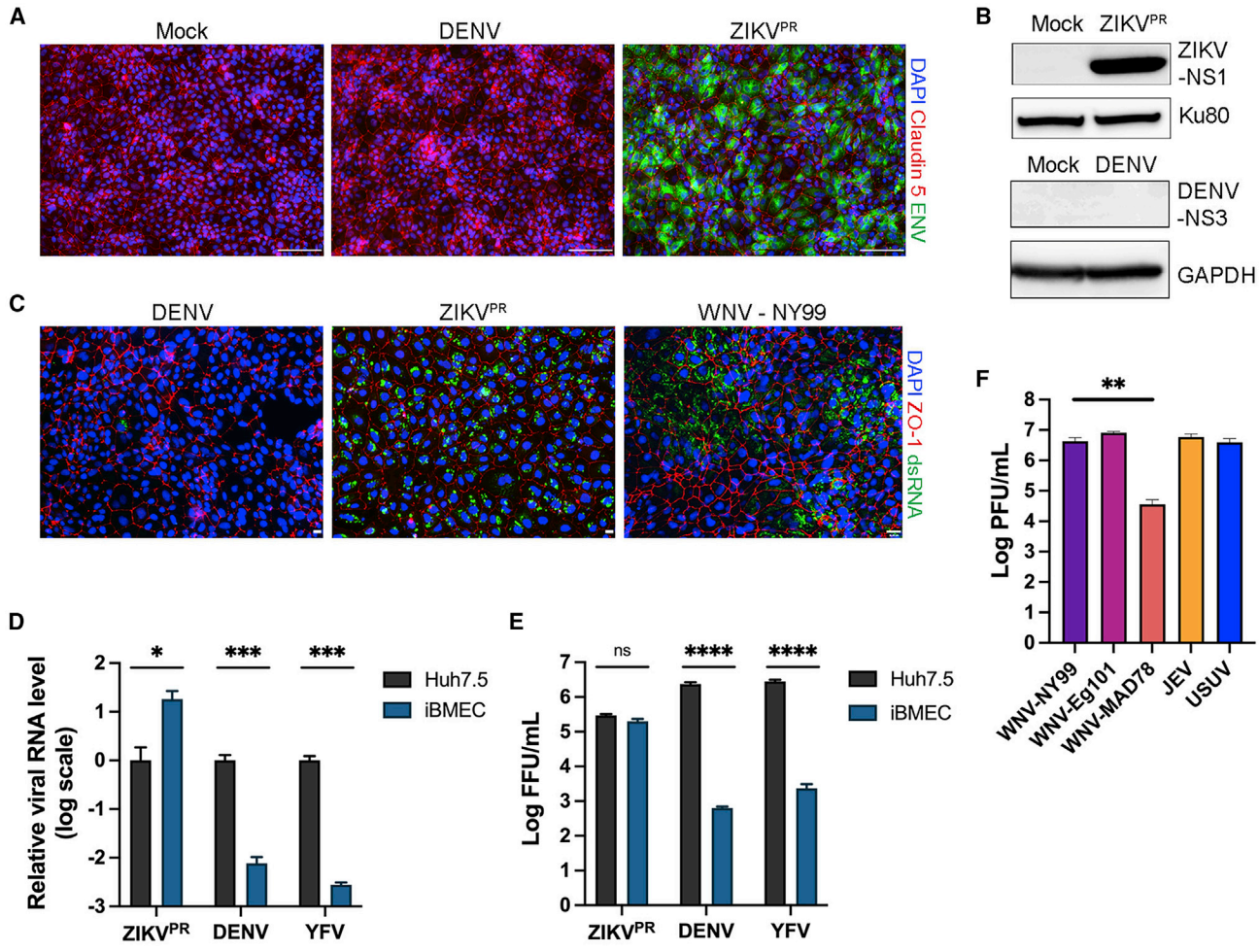

Figure 3. Differential infection of the iBMECs by neurotropic versus non-neurotropic flaviviruses

(A) Representative images of H9-iBMECs infected with DENV-2 (16681) and ZIKV^{PR} at MOI = 1. Cells were fixed at 48 hpi for staining. Scale bars, 100 μm.

(B) Representative western blot images of H9-iBMECs infected with DENV-2 and ZIKV^{PR} at MOI = 1. Cells were lysed at 48 hpi.

(C) Representative images of the H9-iBMECs infected with DENV-2, ZIKV^{PR}, and WNV-NY99 at MOI = 1. Cells were fixed at 48 hpi for staining. Scale bars, 18 μm.

(D and E) Quantification of infection by (D) qRT-PCR and (E) virus titer in Huh7.5 and H9-iBMECs. Cells were infected at MOI = 1, and analysis of (D) intracellular viral RNA and (E) virus production was conducted 48 hpi. Virus titers were quantified as focus-forming units (FFU). Values are mean ± SD from three independent experiments. A two-way ANOVA was performed.

(F) Virus production in IMR-iBMECs infected with flaviviruses. Supernatants from the upper chamber of the transwell were collected at 48 hpi for PFU assay. Values are mean ± SD from three biological replicates. A Student's t test was performed.

this, we cocultured Vero cells with iBMECs in the same well, and the confluent monolayer was then challenged with DENV-2. The iBMECs remained refractory to DENV-2 infection even when neighboring Vero cells were readily infected (Figure 5A), demonstrating the intrinsic nature of the selective resistance to DENV by the iBMECs. Constitutive expression of select antiviral ISGs contributes to viral restriction in PSCs (Wu et al., 2018), which led us to profile the expression of antiviral ISGs in the iBMECs (Figure S5A). Huh7.5 and HUVECs were used as control cells because they did not exhibit a differential infection phenotype for DENV or ZIKV (Figure S5B). We found that the iBMECs express a high endogenous level of IFITM1 compared with Huh7.5 and HUVECs (Figures 5B and S5A). Treatment of HUVECs with IFN induced the expression of IFITM1 and suppressed DENV infection (Figure S5C). Primary human BMECs (hBMECs) also constitutively expressed IFTIM1 (Figures S5D and S5E). Knockout of IFITM1 restored efficient DENV infection of the iBMECs (Figure 5C), demonstrating that the constitutive expression of IFITM1 in iBMECs accounts for the selective inhibition of DENV. We next expressed IFITM1 ectopically in SNB-19 cells, which exhibit an undetectable endogenous level of IFITM1 (Figure 5E). IFITM1 had no inhibitory effect on ZIKV infection but significantly reduced DENV infection (Figures 5D, 5E, and S6A). DENV infection was also strongly inhibited in HEK-293T cells transfected with an IFITM1-expressing plasmid (Figures S6B and S6C). To rule out the possibility that IFITM1 overexpression triggered secretion of other antiviral factors, we cocultured the IFITM1-expressing SNB-19 cells with the unmodified SNB-19

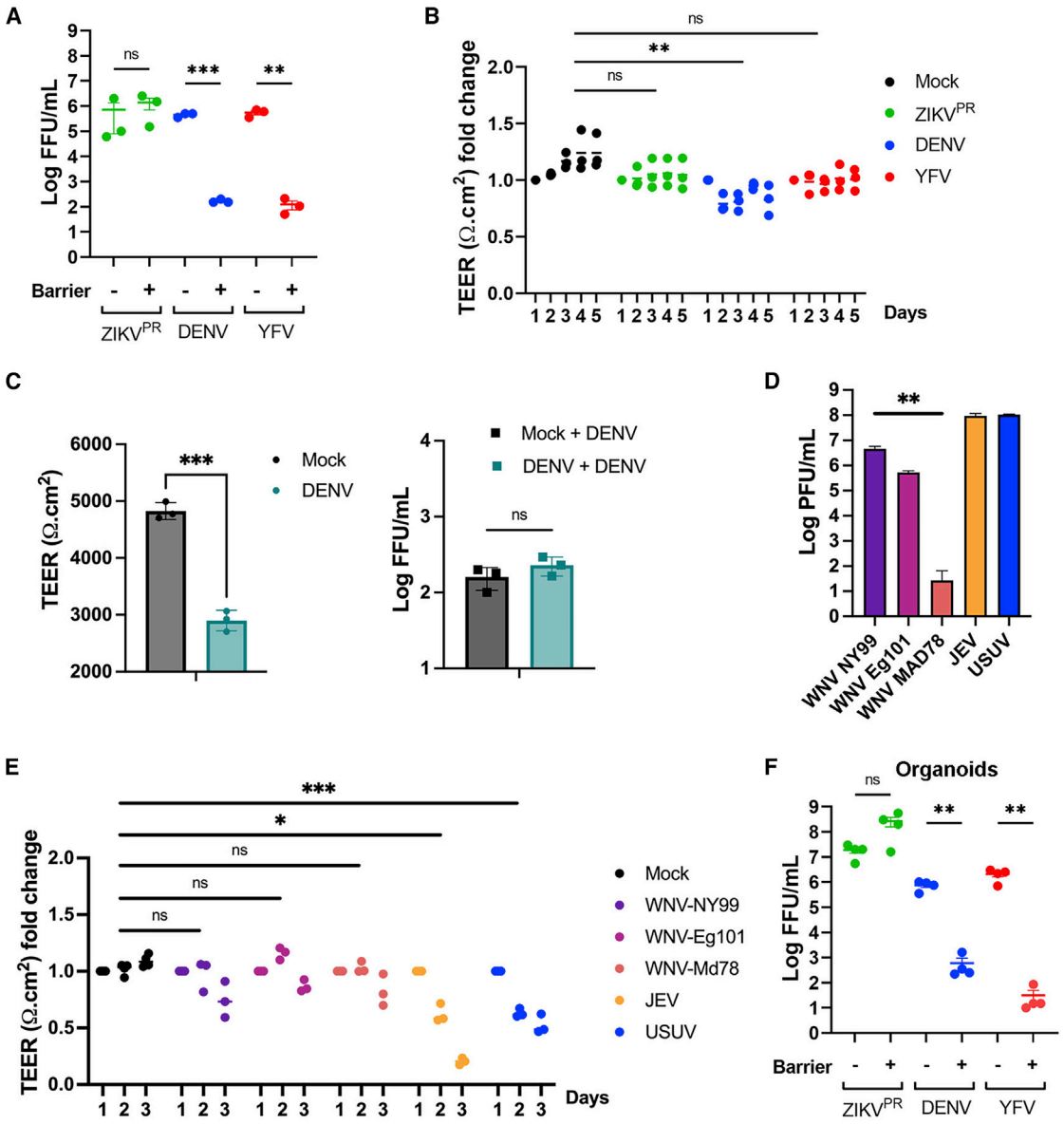

Figure 4. The iBMEC barrier blocks transendothelial infection of CNS cells by non-neurotropic flaviviruses

(A) Virus production by astrocytes exposed to flaviviruses with or without an iBMEC barrier. Astrocytes were cultured in the lower chamber with or without an IMR-iBMEC monolayer for 24 h before virus inoculum (MOIs: ZIKV^{PR} = 1; DENV-2 = 3; YFV = 3) was added to the upper chamber. Supernatants from the lower chamber were collected 48 hpi. Virus titers were quantified as FFU. A Student's t test was performed.

(B) TEER of IMR-iBMEC monolayers exposed to flaviviruses. TEER from iBMECs in (A) were measured immediately before virus addition (day 1) and every day thereafter. Values were normalized to the day-1 values. A two-way ANOVA was performed.

(C) Effect of TEER reduction by DENV on its access to lower chamber. Left panel: TEER value 1 day after exposure to DENV at MOI = 1. Right panel: titer of DENV produced from the day-1 mock- or DENV-infected cells (left panel, at the onset of TEER decrease) exposed to a second inoculum of DENV at MOI = 1. Finally, the virus was collected 48 h after the second inoculation for titration.

(D) Virus production by astrocytes. Astrocytes were cultured in the lower chamber with the IMR-iBMEC monolayer for 24 h before virus inoculum (MOI = 1) was added to the upper chamber. Supernatants from the lower chamber were collected 48 hpi. Virus titers were quantified as PFU, and values are shown as mean ± SD from three biological replicates. A Student's t test was performed.

(E) TEER of IMR-iBMEC monolayers exposed to flaviviruses. TEER from iBMECs in (C) were measured immediately before virus addition (day 1) and every day thereafter. Values were normalized to the day-1 values. A two-way ANOVA was performed.

(F) Virus production by organoids with or without an iBMEC barrier. Day-55 organoids were added to the lower chamber with or without an IMR-iBMEC monolayer along with virus inoculum. Supernatants from the lower chamber were collected 48 hpi. Virus titers were quantified as FFU. A Student's t test was performed.

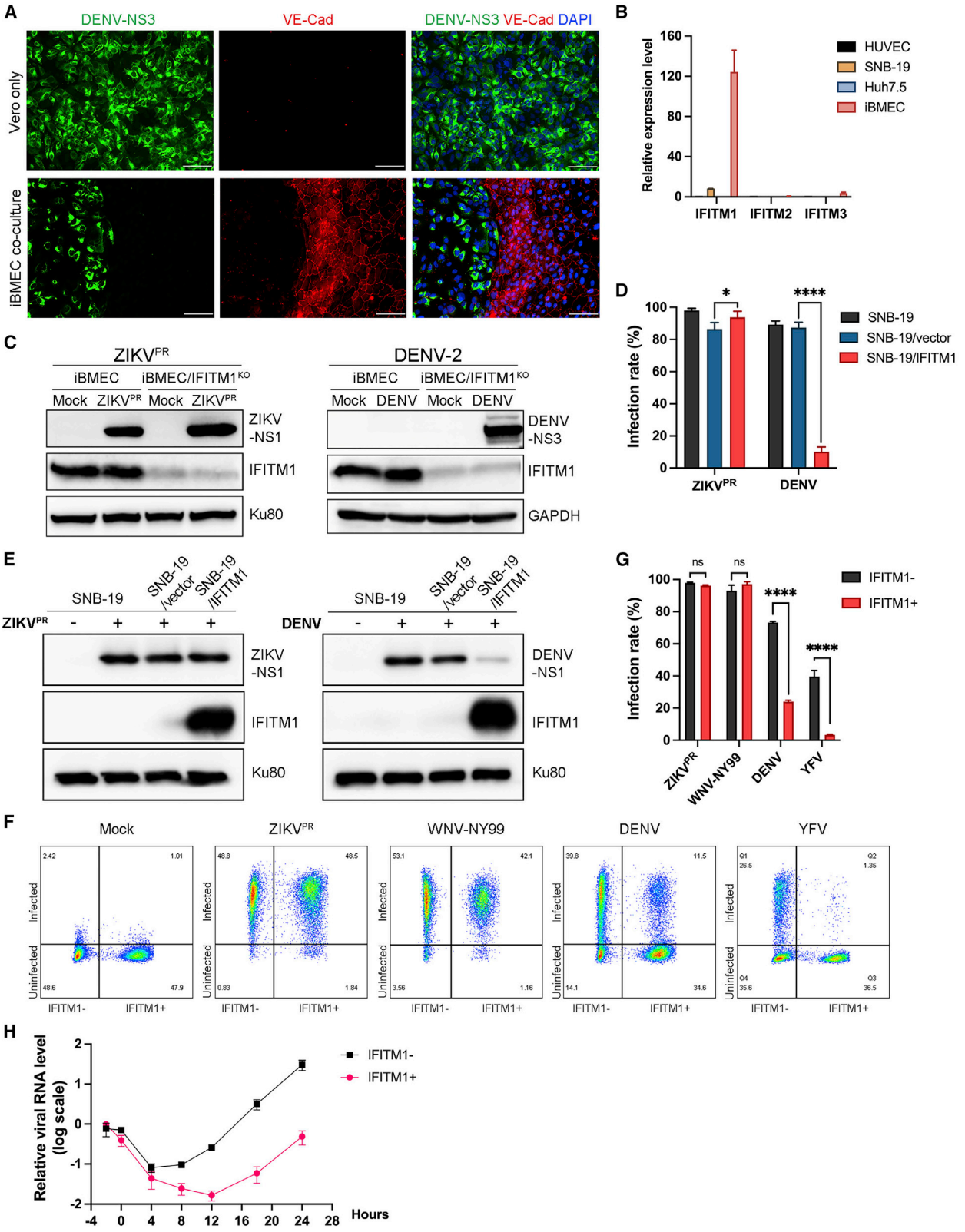

(legend on next page)

cells before infection. A single cell clone (C1-3) that expressed a level of IFITM1 comparable with that of primary hBMECs (Figures S6D–S6F) was used in this experiment to minimize a potential artifact due to high expression. While DENV and YFV-17D infections were inhibited by the expression of IFITM1, no significant difference was observed between the IFITM1-expressing and the unmodified SNB-19 cells regarding the infection efficiency of ZIKV or WNV (Figures 5F, 5G, and S6G). These results demonstrate that IFITM1 can selectively restrict DENV-2 and YFV-17D when expressed in a non-BMEC cell line. IFITM1 expression also had no significant effect on the alphaviruses tested in this study (Figure S5H). To determine the stage of DENV life cycle that is restricted by IFITM1, we performed a time-course experiment and found that IFITM1-expressing SNB-19 cells showed a defect in DENV infection at an early stage (Figure 5H).

Primary human SerCs and RMECs constitutively express IFITM proteins and are selectively resistant to DENV-2 infection

ZIKV is unique among flaviviruses in that it can persist in the male reproductive tract and be sexually transmitted; it can also cause ocular abnormalities in microcephalic infants (Pierson and Diamond, 2018). These properties point to ZIKV's potential ability to also penetrate the BTB and the BRB, a hypothesis that is supported by both *in vivo* and *in vitro* data (Govero et al., 2016; Ma et al., 2017; Matusali et al., 2018; Roach and Alcendor, 2017; Salinas et al., 2017; Siemann et al., 2017; Singh et al., 2017; Uraki et al., 2017). To test whether IFITMs play a role in restricting virus infection for these additional blood-tissue barriers, we examined the expression of IFITM mRNA (Figure 6A) and protein (Figures 6B and 6C) in these cells. SerCs expressed IFITM-1, -2, and -3, while RMECs expressed IFITM-2 and -3 but not IFITM1. The RPE cells expressed IFITM3 RNA at a low level but had no expression of IFITM-1 or -2 at the RNA or protein level. There is a discrepancy of the relative IFITM3 expression between the mRNA and protein levels, the reason for which is unclear at this time but may be due to post-translational regulation in these different cell types. Of the three cell types, the SerCs and RMECs showed minimal sensitivity to DENV-2 infection but both were efficiently infected by ZIKV. Both viruses infected RPE cells equally well, as previously reported (Salinas et al., 2017; Siemann et al., 2017; Singh et al., 2018) (Figure 6D). We observed more than a 100-fold reduction in DENV-2 titers produced by SerCs and RMECs when compared with that produced by Huh7.5 cells, while the ZIKV titer was not reduced in the barrier cells (Figures 6E and 6F). Coculture of the DENV-resistant barrier cells (SerCs or RMECs) with Huh7.5 cells showed that DENV infection is again intrinsically restricted in the barrier cells in a cell-autonomous manner (Figures 6G, 6H, and S7). Because the SerCs express all three IFITM proteins, we performed a broad knockout (KO) of all three genes as well as a single IFITM1 KO (Figure 6I). Both the single and triple KOs increased DENV-2 infection, with the triple KO having a larger effect as measured by protein expression (Figure 6J), infection rate (Figure 6K), and virus production (Figure 6L). Taken together, these results suggest that the constitutive expression of cell-autonomous antiviral factors such as IFITMs can be a common mechanism of viral restriction shared by barrier cells.

DISCUSSION

Here we demonstrated that the iBMECs faithfully recapitulate the neuroinvasiveness of viruses and with this model, we discovered an antiviral mechanism utilized by blood-tissue barriers. Our study highlights the power of stem cell-derived models for advancing understanding of virus-host interactions relevant to viral virulence, pathogenesis, and innate immunity. Stem cell-derived models are attractive when isolation of primary cells faces ethical and technical obstacles as in the case of human CNS cells. PSC-derived hNPCs, glial cells, and brain organoids have been widely adopted for ZIKV research and drug discovery (Cugola et al., 2016; Dang et al., 2016; Garcez et al., 2016; Mesci et al., 2018; Muffat et al., 2018; Qian et al., 2016; Sutarjono, 2019; Tang et al., 2016). Similarly, PSC-derived CNS cells helped to provide insights about the latency and reactivation of herpesviruses (Lafaille et al., 2012, 2019; Zimmer et al., 2018). The differentiated cells have normal karyotypes and are maintained in an environment of carefully curated developmental cues. As a result, these cells are more physiologically relevant than immortalized cell lines, a feature that can be important for viruses that are difficult to culture *in vitro*. The application of human intestinal stem cell-derived enteroids, which combine differentiation with three-dimensional cell organization (Sato et al., 2011), enabled productive infection by the difficult-to-culture human norovirus in enterocytes (Ettayebi et al., 2016). Of note, compared with iBMECs, hCMEC/D3 exhibited low barrier parameters and did not differentiate neuroinvasive versus non-neuroinvasive viruses (data not shown). The transitional nature of the differentiation provides an excellent opportunity to investigate host factors for

Figure 5. The iBMECs intrinsically express IFITM1, which restricts DENV but not ZIKV infection

(A) Representative images of mixed culture of H9-iBMECs and Vero cells challenged with DENV-2. Mixed cells were cultured in the same well and fixed at 48 hpi. MOI = 1. Areas of either only Vero cells (top) or a mixed population (bottom) on the same slide are shown. Scale bars, 100 μm.

(B) mRNA expression levels of IFITM1, IFITM2, and IFITM3. Values are shown as mean ± SD from three biological replicates.

(C) Western blot analysis of DENV-2 and ZIKV infection in H9-iBMECs with or without IFITM1^{KO}. Cell lysates were collected at 48 hpi. MOI = 1.

(D and E) Analysis of DENV-2 and ZIKV^{PR} infection in SNB-19 cells that ectopically express IFITM1. Results shown are (D) infection rates and (E) NS1 expression. SNB-19 cells were stably transduced with a GFP-tagged lentiviral vector expressing IFITM1 before infection at MOI = 1. Cells were collected at 24 hpi.

(F and G) Flow cytometry analysis of flavivirus infection of SNB-19 cells with or without IFITM1 expression. SNB-19 cells and IFITM1-expressing single-cell clone C1-3 cells were mixed and plated in the same well for infection at MOI = 1. Cells were stained at 24 hpi. Data shown as (F) representative FACS profiles and (G) infection rate.

(H) DENV RNA level in SNB-19 cells with or without IFITM1. Cells were inoculated with DENV on ice (−2 h) for 2 h before shifting to 37°C (0 h). MOI = 1. Cell pellets were collected at indicated times. Values were normalized to GAPDH and then to the mean values of the −2 h time point. Values are shown as mean ± SD from three biological replicates. A two-way ANOVA was performed.

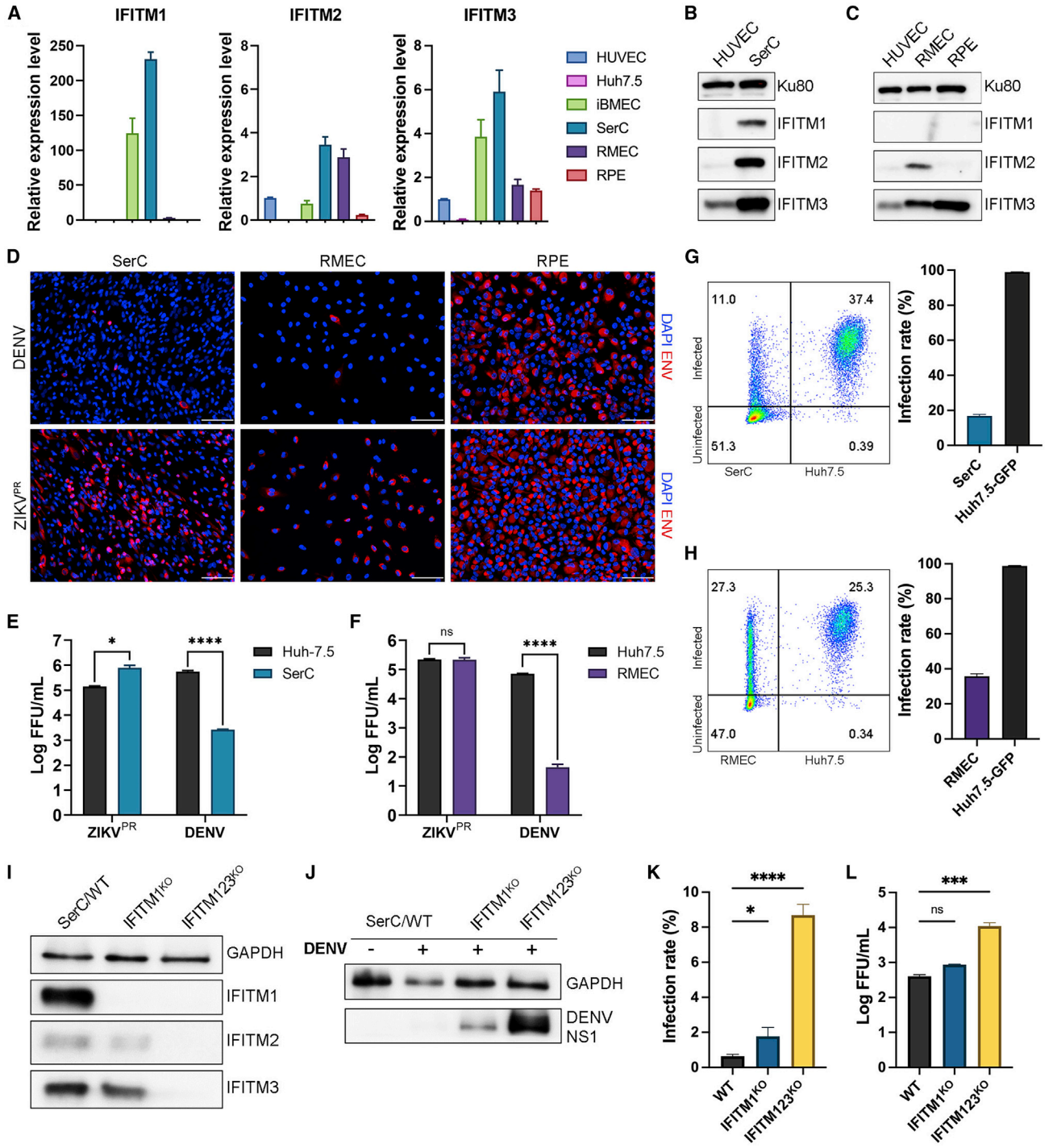

Figure 6. Primary human SerCs and RMECs constitutively express IFITM proteins and are selectively resistant to DENV infection

(A) mRNA expression of IFITMs.

(B and C) Western blot analysis of protein expression of IFITMs in (B) BTB and (C) BRB cells.

(D) Infection of the three types of barrier cells by DENV-2 and ZIKV^{PR}. Cells were infected at MOI = 1 and collected 48 hpi for staining. Scale bars, 100 μm.

(E and F) Viral production by (E) SerCs and (F) RMECs in comparison with Huh7.5 cells. Supernatants were collected 48 hpi. MOI = 1. Virus titers were quantified as FFUs. A two-way ANOVA was performed.

(G and H) Flow cytometry analysis of DENV-2 infection of (G) SerCs and (H) RMECs cocultured with Huh7.5-GFP cells. SerCs or RMECs were mixed with GFP-tagged Huh7.5 cells and plated in the same well for infection with DENV-2 at MOI = 1. Cells were stained at 48 hpi.

(legend continued on next page)

viruses with narrow tropisms. For example, experiments with differentiated human hepatocyte-like cells revealed a defined transition to hepatitis C virus permissiveness and led to the discovery that IFN-independent expression of ISGs protects stem cells from viral infection (Wu et al., 2012, 2018).

We also demonstrated that the iBMEC monolayer responds to signals that regulate BBB tightness *in vivo*. Treating the monolayer at the basolateral side with MCP-1 and TNF-α increased transendothelial migration of monocytes. The iBMECs also respond to LPS and IFN-λ, two known regulators of BBB permeability (Daniels et al., 2014; Eckman et al., 1958; Kraus et al., 2004; Lazear et al., 2015), congruent with results from *in vivo* experiments (Daniels et al., 2014; Lazear et al., 2015). In addition to immune and inflammatory signaling, the interaction between BMEC and brain parenchyma is important in BBB regulation. With the combination of IMR90 as the stem cell source and primary human astrocytes as a coculture, the iBMEC monolayer exhibited a TEER as high as 5,175 $\Omega.cm^2$, approaching the *in vivo* values measured in rats (Butt et al., 1990) or estimated for humans (Lauschke et al., 2017). In contrast, the hCMEC/D3 monolayer exhibits TEER values in the range of 60–350 $\Omega.cm^2$ under various conditions (Boyer-Di Ponio et al., 2014; Bramley et al., 2017; Daniels et al., 2013; Lippmann et al., 2012), similar to that of the human primary BMECs (Daniels et al., 2013; Lippmann et al., 2012; Paradis et al., 2016). The iBMECs, with or without primary astrocytes, typically exhibit TEER values in the range of 600–2,000 $\Omega.cm^2$ (Lippmann et al., 2012, 2014; Ohshima et al., 2019) but complex cocultures that include additional components, such as pericytes and neurons, can produce values over 5,000 $\Omega.cm^2$ (Hollmann et al., 2017; Lippmann et al., 2014; Neal et al., 2019).

The coculture model enabled us to investigate both direct virus infection of ECs followed by basolateral release and the disruption of BBB integrity as distinct but not mutually exclusive mechanisms of CNS access. DENV and YFV-17D were inefficient in infecting the iBMECs to access the astrocytes for infection; ZIKV infects the iBMECs and reaches the lower chamber but does not significantly alter the monolayer TEER; JEV and USUV infect the iBMECs and readily disrupt the barrier. There are also clear differences between the three strains of WNV tested. NY99 is neuroinvasive and neurovirulent (Beasley et al., 2002) while Eg101 is neuroinvasive but replicates to a low level in the brain and is avirulent (Beasley et al., 2002; Kumar et al., 2016). Both strains behaved similarly to JEV and USUV in the iBMECs model. In contrast, WNV-MAD78, an avirulent and non-neuroinvasive strain (Beasley et al., 2002), is much less efficient in getting across the iBMEC barrier and infecting astrocytes. A defect in infecting astrocytes was also reported using primary human BMECs (Hussmann et al., 2013). In that study, the MAD78 strain was nevertheless able to get across the monolayer of the primary BMECs in the absence of astrocytes. It is not clear whether the difference in monolayer tightness contributed to this result, as the TEER values of the primary BMEC monolayer were only in the range of 250–300 $\Omega.cm^2$ (Hussmann et al., 2013). Many neurotropic viruses, including the ones studied here, can potentially use multiple mechanisms for gaining access to the CNS (Diamond and Klein, 2004; Hsieh and St John, 2020; Jurado et al., 2018; Mladinich et al., 2017; Tamhankar and Patterson, 2019), but a non-neuroinvasive virus should be deficient in deploying any of these and other possible mechanisms. With a large dynamic range of TEER values, permissiveness to monocyte migration, and differential susceptibility to neuroinvasive and non-neuroinvasive viruses, the iBMEC-BBB represents a valuable model for studying the broad mechanisms of CNS invasion through this barrier.

We were able to mimic the *in vivo* neuroinvasive phenotype of alphaviruses in the iBMEC-BBB model. We found that both M190 and K260 in the E2 glycoprotein are required for efficient SINV replication and production in iBMECs. These residues may allow the neuroinvasive SVNI strain to engage with a BMEC-specific cell-surface receptor, resulting in efficient infection of BMECs. Structural studies (Li et al., 2010; Voss et al., 2010) indicate that M190 is located in domain B of E2, which is essential for cell recognition and attachment, while K260 is located in the β-ribbon area between domains B and C. Our result suggests that the K190M mutation in the non-neuroinvasive SVN strain may affect E2 binding to cell-surface molecules, leading to the change in viral tropism. The E260K mutation alone does not confer neuroinvasive capability on SVN but helped to fully restore infection of the iBMECs by the K190M mutant. It will be interesting to determine whether K260 synergizes with the cell-surface binding mediated by domain B. In addition, even though the replication of the SVN strain with both E2 mutations (E2M2) is comparable with that of R47, E2M2 viral production is lower than that of SVNI, suggesting that the U8G mutation might play a role in viral release. iBMECs represent an excellent *in vitro* model for conducting further studies to pursue this intriguing possibility.

DENV can cause neurological manifestations in some severe cases (Carod-Artal et al., 2013). Whether this relatively uncommon outcome is due to a direct infection of the BBB cells is not clear. Conceivably even a subtle difference in entry routes can influence the extent of inhibition conferred by the IFITMs (Li et al., 2013; Spence et al., 2019; Suddala et al., 2019). The isolates from all four serotypes of DENV that we used in this study failed to productively infect the iBMECs *in vitro*. However, the fact that only two amino acid changes in the envelope protein of an alphavirus can completely change the infection outcome suggests that it should be possible for certain isolates of non-neuroinvasive viruses to gain the ability to infect BMECs. Clinically, a high level of viremia in severe dengue cases may also lead to a high level of NS1 in blood, which can compromise endothelial integrity (Beatty et al., 2015; Biering et al., 2021; Pan et al., 2021; Puerta-Guardo et al., 2019; Wessel et al., 2021).

(I) Western blot analysis of IFITM protein expression in IFITM KO SerCs. SerCs were stably transduced with a lentiviral vector expressing guide RNAs targeting either IFITM1 only ($IFITM1^{KO}$) or all three members of antiviral IFITMs ($IFITM123^{KO}$).

(J–L) Analysis of DENV-2 infection in SerCs with IFITM KO by (J) western blotting, (K) flow-cytometry-based quantification, and (L) FFU assay. Wild-type or KO cells were infected with DENV-2 at MOI = 1 and collected 48 hpi. A one-way ANOVA was performed.

Values are mean ± SD from three independent experiments.

Of the five human IFITM family members, IFITM1, IFITM2, and IFITM3 have broad antiviral activities both *in vitro* and *in vivo* (Liao et al., 2019; Perreira et al., 2013; Zhao et al., 2018). Although IFITMs have an antiviral effect against DNA viruses and non-enveloped RNA viruses (Anafu et al., 2013; Li et al., 2018; Munoz-Moreno et al., 2016; Xu et al., 2014; Zhu et al., 2013), the main targets of these IFITMs are enveloped RNA viruses (Perreira et al., 2013) such as flaviviruses (Brass et al., 2009; Chen et al., 2017; Gorman et al., 2016; Jiang et al., 2010; Savidis et al., 2016). The relative effectiveness of virus inhibition by the IFITMs varies, but IFITM3 typically exhibits the strongest and broadest inhibition (Bailey et al., 2012; Everitt et al., 2012, 2013; Gorman et al., 2016; Poddar et al., 2016). In contrast, IFITM1 and IFITM2 are less characterized in their *in vivo* function and potency against different viruses. Here we show that IFITM1 constitutively expressed in iBMECs can selectively inhibit non-neuroinvasive flaviviruses, a result further supported by ectopic expression experiments in a cell line that normally lacks IFITM1 constitutive expression. In a previous study on the anti-ZIKV function of IFITMs (Savidis et al., 2016), IFITM1 overexpressed in A549 cells had a modest inhibitory effect on ZIKV infection, but the inhibition was much lower than that of IFITM3 and more comparable with an IFITM3 mutant without the proper subcellular localization (Chesarino et al., 2014; Jia et al., 2014). In another study, an inhibitory effect of IFITM1 expression on WNV virus-like particles (VLPs) was observed in Vero E6 cells but its effect on infectious wild-type WNV was not tested, whereas expression of IFITM3 inhibited both VLPs and infectious WNV in the same study (Brass et al., 2009). Multiple factors can influence the degree of virus suppression by IFITMs or other ISGs in cell-culture systems. These include ISG expression levels, alone or relative to the amount of virus input (Spence et al., 2019), or other cell-type-specific differences. We observed that ectopic expression of IFITM1 in Huh7.5 cells was unable to inhibit even DENV-2 or YFV-17D under the same conditions as the SNB-19 experiments. Determination of whether this is due to the defects in the IFN activation pathway in the Huh7.5 cells (Binder et al., 2007; Blight et al., 2002; Sumpter et al., 2005) or a difference in subcellular localization of the IFITM1 protein in these cells (data not shown) requires additional experimentation.

The mechanism of the IFITM antiviral function has been studied extensively, and the majority of the studies point to inhibition at the membrane fusion step (Li et al., 2013; Spence et al., 2019; Suddala et al., 2019). Our data are consistent with this mechanism and prior studies on Flaviviridae (Brass et al., 2009; Narayana et al., 2015; Wilkins et al., 2013), suggesting that the mechanism by which ZIKV and other neuroinvasive flaviviruses escape IFITM1-mediated restriction likely involves an alternative route/location of virus envelope fusion. Interestingly, JEV has been shown to use distinct endocytic routes for entry in neuronal versus non-neuronal cells (Kalia et al., 2013). Such a mechanism, if applicable to related neurotropic flaviviruses, may account for their resistance to IFITM1. It is also possible that the non-sensitive viruses have developed active countermeasures to neutralize IFITMs given the frequent use of these antiviral factors as the intrinsic immune mediators protecting vital cells and tissues from virus infection (Bailey et al., 2012; Bedford et al., 2019; Popson et al., 2014; Wakim et al., 2013; Wu et al., 2018).

How ISGs are expressed in an IFN-independent manner in specific cell types is unknown. We found that freshly purified human primary BMECs constitutively express a high level of IFITM1 but its expression decreases significantly upon *in vitro* passage (data not shown). Data in PSCs suggest that epigenetic regulations may be involved (Wu et al., 2018), but because the iBMECs are highly differentiated, the mechanism for the intrinsic expression of IFITM1 may be distinct. A recent study reported a global gene profile change in iBMECs upon an additional step of endothelial maturation, but there is no significant change in IFITM1 (Lu et al., 2021), suggesting its expression mechanism is conserved in iBMECs with or without this step. SerCs are also highly differentiated but constitutively express the three IFITMs (this study) and several other ISGs (Dejucq et al., 1998). It is plausible that the specialized barrier cells such as BMECs, SerCs, and RMECs share common mechanisms for the IFN-independent expression of ISGs for the purpose of limiting virus access to immune-privileged sites.

Limitations of the study

The technical limitations of the study include the inability of the model to capture complex multicellular interactions and the lack of high-resolution vascular structure for the *in situ* detection of IFITM1 expression. Although the model accurately recapitulates the *in vivo* viral CNS invasion phenotypes of the alphavirus mutants, the molecular mechanism by which these mutations enhance iBMEC infection remains unclear. In addition, unequivocal evidence for productive infection of brain endothelial cells *in vivo* by many of these viruses is yet to be demonstrated.

STAR★METHODS

Detailed methods are provided in the online version of this paper and include the following:

- KEY RESOURCES TABLE
- RESOURCE AVAILABILITY
  - Lead contact
  - Materials availability
  - Data and code availability
- EXPERIMENTAL MODEL AND SUBJECT DETAILS
  - Cell lines
  - Organoids
- METHOD DETAILS
  - Differentiation of iBMECs from human pluripotent stem cells
  - Differentiation of cortical neural progenitor cells from hiPSCs
  - Tube formation assay
  - Measurement of transepithelial/endothelial electrical resistance (TEER)
  - Monocyte migration assay
  - Sodium fluorescein assay
  - Efflux transporter assay
  - SINV full-length cDNA plasmids and SVN cDNA mutant construction

- Alphavirus propagation, titration, and infection
- Flavivirus propagation and infection
- Titration of flaviviruses
- Generation of IFITM1-expressing cell lines
- CRISPR knockout of IFITM proteins
- Time-course experiment of DENV infection in IFITM1-expressing cells
- Cell coculture experiments
- Cytokine multiplex analysis
- Immunofluorescence assay
- Immunofluorescence assay for astrocytes in transwell setups
- Immunofluorescence staining of brain cerebral cortex tissue sections
- Flow cytometry
- Western blotting
- Quantitative real-time RT-PCR

● QUANTIFICATION AND STATISTICAL ANALYSIS

SUPPLEMENTAL INFORMATION

Supplemental information can be found online at https://doi.org/10.1016/j.celrep.2022.110885.

ACKNOWLEDGMENTS

This study was supported by National Institutes of Health grants to H.T. (U19 AI131130 and R01AI146342), M.M.H.L. (R01AI158704), M.A.B. (U19AI131130), M.K. (R21OD024896), G.M. (U19AI131130 and R35NS097370), and H.S. (R35NS116843). M.M.H.L. is also supported by UCLA Broad Stem Cell Research Center (Research Award).

AUTHOR CONTRIBUTIONS

Conception and design, H.T., Y.C., A.M., M.M.H.L., and J.L.; performing experiments and collection of data, Y.C., A.M., Z.Y., M.B., M.A.B., J.L., J.P.N., E.S., M.B.N., and M.K.; contribution of reagents, C.X., X.Q., P.T.T.N., Z.W., H.S., G.-L.M., M.A.B., and M.K.; analysis and interpretation of data, H.T., Y.C., A.M., M.M.H.L., M.A.B., and M.K.; manuscript writing, H.T., Y.C., and A.M. wrote the initial draft of the paper; M.M.H.L., M.A.B., Z.Y., and M.K. provided edits; all authors read the manuscript.

DECLARATION OF INTERESTS

The authors declare no competing interests.

Received: September 24, 2021
Revised: March 27, 2022
Accepted: May 5, 2022
Published: May 31, 2022

REFERENCES

Abbott, N.J., Ronnback, L., and Hansson, E. (2006). Astrocyte-endothelial interactions at the blood-brain barrier. Nat. Rev. Neurosci. *7*, 41–53. https://doi.org/10.1038/nrn1824.

Alimonti, J.B., Ribecco-Lutkiewicz, M., Sodja, C., Jezierski, A., Stanimirovic, D.B., Liu, Q., Haqqani, A.S., Conlan, W., and Bani-Yaghoub, M. (2018). Zika virus crosses an in vitro human blood brain barrier model. Fluids Barriers CNS *15*, 15. https://doi.org/10.1186/s12987-018-0100-y.

Anafu, A.A., Bowen, C.H., Chin, C.R., Brass, A.L., and Holm, G.H. (2013). Interferon-inducible transmembrane protein 3 (IFITM3) restricts reovirus cell entry. J. Biol. Chem. *288*, 17261–17271. https://doi.org/10.1074/jbc.M112.438515.

Atkins, G.J., and Sheahan, B.J. (2016). Molecular determinants of alphavirus neuropathogenesis in mice. J. Gen. Virol. *97*, 1283–1296. https://doi.org/10.1099/jgv.0.000467.

Bailey, C.C., Huang, I.C., Kam, C., and Farzan, M. (2012). Ifitm3 limits the severity of acute influenza in mice. Plos Pathog. *8*, e1002909. https://doi.org/10.1371/journal.ppat.1002909.

Bayer, A., Lennemann, N.J., Ouyang, Y., Bramley, J.C., Morosky, S., Marques, E.T., Jr., Cherry, S., Sadovsky, Y., and Coyne, C.B. (2016). Type III interferons produced by human placental trophoblasts confer protection against Zika virus infection. Cell Host Microbe *19*, 705–712. https://doi.org/10.1016/j.chom.2016.03.008.

Beasley, D.W., Li, L., Suderman, M.T., and Barrett, A.D. (2002). Mouse neuroinvasive phenotype of West Nile virus strains varies depending upon virus genotype. Virology *296*, 17–23. https://doi.org/10.1006/viro.2002.1372.

Beatty, P.R., Puerta-Guardo, H., Killingbeck, S.S., Glasner, D.R., Hopkins, K., and Harris, E. (2015). Dengue virus NS1 triggers endothelial permeability and vascular leak that is prevented by NS1 vaccination. Sci. Transl. Med. *7*, 304ra141. https://doi.org/10.1126/scitranslmed.aaa3787.

Bedford, J.G., O'Keeffe, M., Reading, P.C., and Wakim, L.M. (2019). Rapid interferon independent expression of IFITM3 following T cell activation protects cells from influenza virus infection. PLoS One *14*, e0210132. https://doi.org/10.1371/journal.pone.0210132.

Bick, M.J., Carroll, J.W.N., Gao, G., Goff, S.P., Rice, C.M., and MacDonald, M.R. (2003). Expression of the zinc-finger antiviral protein inhibits alphavirus replication. J. Virol. *77*, 11555–11562. https://doi.org/10.1128/jvi.77.21.11555-11562.2003.

Biering, S.B., Akey, D.L., Wong, M.P., Brown, W.C., Lo, N.T.N., Puerta-Guardo, H., Tramontini Gomes de Sousa, F., Wang, C., Konwerski, J.R., Espinosa, D.A., et al. (2021). Structural basis for antibody inhibition of flavivirus NS1-triggered endothelial dysfunction. Science *371*, 194–200. https://doi.org/10.1126/science.abc0476.

Binder, M., Kochs, G., Bartenschlager, R., and Lohmann, V. (2007). Hepatitis C virus escape from the interferon regulatory factor 3 pathway by a passive and active evasion strategy. Hepatology *46*, 1365–1374. https://doi.org/10.1002/hep.21829.

Blight, K.J., McKeating, J.A., and Rice, C.M. (2002). Highly permissive cell lines for subgenomic and genomic hepatitis C virus RNA replication. J. Virol. *76*, 13001–13014. https://doi.org/10.1128/jvi.76.24.13001-13014.2002.

Ponio, J.B.D., El-Ayoubi, F., Glacial, F., Ganeshamoorthy, K., Driancourt, C., Godet, M., Perriere, N., Guillevic, O., Couraud, P.O., and Uzan, G. (2014). Instruction of circulating endothelial progenitors in vitro towards specialized blood-brain barrier and arterial phenotypes. PLoS One *9*, e84179. https://doi.org/10.1371/journal.pone.0084179.

Bramley, J.C., Drummond, C.G., Lennemann, N.J., Good, C.A., Kim, K.S., and Coyne, C.B. (2017). A three-dimensional cell culture system to model RNA virus infections at the blood-brain barrier. mSphere *2*, e00206-17. https://doi.org/10.1128/mSphere.00206-17.

Brass, A.L., Huang, I.C., Benita, Y., John, S.P., Krishnan, M.N., Feeley, E.M., Ryan, B.J., Weyer, J.L., van der Weyden, L., Fikrig, E., et al. (2009). The IFITM proteins mediate cellular resistance to influenza A H1N1 virus, West Nile virus, and dengue virus. Cell *139*, 1243–1254. https://doi.org/10.1016/j.cell.2009.12.017.

Butt, A.M., Jones, H.C., and Abbott, N.J. (1990). Electrical resistance across the blood-brain barrier in anaesthetized rats: a developmental study. J. Physiol. *429*, 47–62. https://doi.org/10.1113/jphysiol.1990.sp018243.

Cain, M.D., Salimi, H., Diamond, M.S., and Klein, R.S. (2019). Mechanisms of pathogen invasion into the central nervous system. Neuron *103*, 771–783. https://doi.org/10.1016/j.neuron.2019.07.015.

Caine, E.A., Scheaffer, S.M., Arora, N., Zaitsev, K., Artyomov, M.N., Coyne, C.B., Moley, K.H., and Diamond, M.S. (2019). Interferon lambda protects the female reproductive tract against Zika virus infection. Nat. Commun. *10*, 280. https://doi.org/10.1038/s41467-018-07993-2.

Campbell, M., and Humphries, P. (2012). The blood-retina barrier: tight junctions and barrier modulation. Adv. Exp. Med. Biol. *763*, 70–84. https://doi.org/10.1007/978-1-4614-4711-5_3.

Carod-Artal, F.J., Wichmann, O., Farrar, J., and Gascon, J. (2013). Neurological complications of dengue virus infection. Lancet Neurol. *12*, 906–919. https://doi.org/10.1016/S1474-4422(13)70150-9.

Chen, S., Wang, L., Chen, J., Zhang, L., Wang, S., Goraya, M.U., Chi, X., Na, Y., Shao, W., Yang, Z., and Zeng, X. (2017). Avian interferon-inducible transmembrane protein family effectively restricts avian tembusu virus infection. Front. Microbiol. *8*, 672. https://doi.org/10.3389/fmicb.2017.00672.

Chesarino, N.M., McMichael, T.M., Hach, J.C., and Yount, J.S. (2014). Phosphorylation of the antiviral protein interferon-inducible transmembrane protein 3 (IFITM3) dually regulates its endocytosis and ubiquitination. J. Biol. Chem. *289*, 11986–11992. https://doi.org/10.1074/jbc.M114.557694.

Cle, M., Barthelemy, J., Desmetz, C., Foulongne, V., Lapeyre, L., Bollore, K., Tuaillon, E., Erkilic, N., Kalatzis, V., Lecollinet, S., et al. (2020). Study of Usutu virus neuropathogenicity in mice and human cellular models. Plos Negl. Trop. Dis. *14*, e0008223. https://doi.org/10.1371/journal.pntd.0008223.

Cugola, F.R., Fernandes, I.R., Russo, F.B., Freitas, B.C., Dias, J.L.M., Guimaraes, K.P., Benazzato, C., Almeida, N., Pignatari, G.C., Romero, S., et al. (2016). The Brazilian Zika virus strain causes birth defects in experimental models. Nature *534*, 267–271. https://doi.org/10.1038/nature18296.

Daneman, R., and Prat, A. (2015). The blood-brain barrier. Cold Spring Harb. Perspect. Biol. *7*, a020412. https://doi.org/10.1101/cshperspect.a020412.

Dang, J., Tiwari, S.K., Lichinchi, G., Qin, Y., Patil, V.S., Eroshkin, A.M., and Rana, T.M. (2016). Zika virus depletes neural progenitors in human cerebral organoids through activation of the innate immune receptor TLR3. Cell Stem Cell *19*, 258–265. https://doi.org/10.1016/j.stem.2016.04.014.

Daniels, B.P., Cruz-Orengo, L., Pasieka, T.J., Couraud, P.O., Romero, I.A., Weksler, B., Cooper, J.A., Doering, T.L., and Klein, R.S. (2013). Immortalized human cerebral microvascular endothelial cells maintain the properties of primary cells in an in vitro model of immune migration across the blood brain barrier. J. Neurosci. Methods *212*, 173–179. https://doi.org/10.1016/j.jneumeth.2012.10.001.

Daniels, B.P., Holman, D.W., Cruz-Orengo, L., Jujjavarapu, H., Durrant, D.M., and Klein, R.S. (2014). Viral pathogen-associated molecular patterns regulate blood-brain barrier integrity via competing innate cytokine signals. mBio *5*, e01476-14. https://doi.org/10.1128/mBio.01476-14.

Daniels, B.P., Jujjavarapu, H., Durrant, D.M., Williams, J.L., Green, R.R., White, J.P., Lazear, H.M., Gale, M., Jr., Diamond, M.S., and Klein, R.S. (2017). Regional astrocyte IFN signaling restricts pathogenesis during neurotropic viral infection. J. Clin. Invest. *127*, 843–856. https://doi.org/10.1172/JCI88720.

Dehouck, M.P., Jolliet-Riant, P., Bree, F., Fruchart, J.C., Cecchelli, R., and Tillement, J.P. (1992). Drug transfer across the blood-brain barrier: correlation between in vitro and in vivo models. J. Neurochem. *58*, 1790–1797. https://doi.org/10.1111/j.1471-4159.1992.tb10055.x.

Dejucq, N., Lienard, M.O., and Jegou, B. (1998). Interferons and interferon-induced antiviral proteins in the testis. J. Reprod. Immunol. *41*, 291–300. https://doi.org/10.1016/s0165-0378(98)00065-5.

Diamond, M.S., and Klein, R.S. (2004). West Nile virus: crossing the blood-brain barrier. Nat. Med. *10*, 1294–1295. https://doi.org/10.1038/nm1204-1294.

Dohgu, S., Takata, F., Yamauchi, A., Nakagawa, S., Egawa, T., Naito, M., Tsuruo, T., Sawada, Y., Niwa, M., and Kataoka, Y. (2005). Brain pericytes contribute to the induction and up-regulation of blood-brain barrier functions through transforming growth factor-beta production. Brain Res. *1038*, 208–215. https://doi.org/10.1016/j.brainres.2005.01.027.

Dubuisson, J., Lustig, S., Ruggli, N., Akov, Y., and Rice, C.M. (1997). Genetic determinants of Sindbis virus neuroinvasiveness. J. Virol. *71*, 2636–2646. https://doi.org/10.1128/JVI.71.4.2636-2646.1997.

Eckman, P.L., King, W.M., and Brunson, J.G. (1958). Studies on the blood brain barrier. I. Effects produced by a single injection of gramnegative endotoxin on the permeability of the cerebral vessels. Am. J. Pathol. *34*, 631–643.

Ettayebi, K., Crawford, S.E., Murakami, K., Broughman, J.R., Karandikar, U., Tenge, V.R., Neill, F.H., Blutt, S.E., Zeng, X.L., Qu, L., et al. (2016). Replication of human noroviruses in stem cell-derived human enteroids. Science *353*, 1387–1393. https://doi.org/10.1126/science.aaf5211.

Everitt, A.R., Clare, S., McDonald, J.U., Kane, L., Harcourt, K., Ahras, M., Lall, A., Hale, C., Rodgers, A., Young, D.B., et al. (2013). Defining the range of pathogens susceptible to Ifitm3 restriction using a knockout mouse model. PLoS One *8*, e80723. https://doi.org/10.1371/journal.pone.0080723.

Everitt, A.R., Clare, S., Pertel, T., John, S.P., Wash, R.S., Smith, S.E., Chin, C.R., Feeley, E.M., Sims, J.S., Adams, D.J., et al. (2012). IFITM3 restricts the morbidity and mortality associated with influenza. Nature *484*, 519–523. https://doi.org/10.1038/nature10921.

Frolova, E.I., Fayzulin, R.Z., Cook, S.H., Griffin, D.E., Rice, C.M., and Frolov, I. (2002). Roles of nonstructural protein nsP2 and Alpha/Beta interferons in determining the outcome of Sindbis virus infection. J. Virol. *76*, 11254–11264. https://doi.org/10.1128/jvi.76.22.11254-11264.2002.

Garcez, P.P., Loiola, E.C., Madeiro da Costa, R., Higa, L.M., Trindade, P., Delvecchio, R., Nascimento, J.M., Brindeiro, R., Tanuri, A., and Rehen, S.K. (2016). Zika virus impairs growth in human neurospheres and brain organoids. Science *352*, 816–818. https://doi.org/10.1126/science.aaf6116.

Gorman, M.J., Poddar, S., Farzan, M., and Diamond, M.S. (2016). The interferon-stimulated gene Ifitm3 restricts West Nile virus infection and pathogenesis. J. Virol. *90*, 8212–8225. https://doi.org/10.1128/JVI.00581-16.

Govero, J., Esakky, P., Scheaffer, S.M., Fernandez, E., Drury, A., Platt, D.J., Gorman, M.J., Richner, J.M., Caine, E.A., Salazar, V., et al. (2016). Zika virus infection damages the testes in mice. Nature *540*, 438–442. https://doi.org/10.1038/nature20556.

Hollidge, B.S., Cohen, C.A., Akuoku Frimpong, J., Badger, C.V., Dye, J.M., and Schmaljohn, C.S. (2021). Toll-like receptor 4 mediates blood-brain barrier permeability and disease in C3H mice during Venezuelan equine encephalitis virus infection. Virulence *12*, 430–443. https://doi.org/10.1080/21505594.2020.1870834.

Hollmann, E.K., Bailey, A.K., Potharazu, A.V., Neely, M.D., Bowman, A.B., and Lippmann, E.S. (2017). Accelerated differentiation of human induced pluripotent stem cells to blood-brain barrier endothelial cells. Fluids Barriers CNS *14*, 9. https://doi.org/10.1186/s12987-017-0059-0.

Hsieh, J.T., Rathore, A.P.S., Soundarajan, G., and St John, A.L. (2019). Japanese encephalitis virus neuropenetrance is driven by mast cell chymase. Nat. Commun. *10*, 706. https://doi.org/10.1038/s41467-019-08641-z.

Hsieh, J.T., and St John, A.L. (2020). Japanese encephalitis virus and its mechanisms of neuroinvasion. PLoS Pathog. *16*, e1008260. https://doi.org/10.1371/journal.ppat.1008260.

Hussmann, K.L., Samuel, M.A., Kim, K.S., Diamond, M.S., and Fredericksen, B.L. (2013). Differential replication of pathogenic and nonpathogenic strains of West Nile virus within astrocytes. J. Virol. *87*, 2814–2822. https://doi.org/10.1128/JVI.02577-12.

Jia, R., Xu, F., Qian, J., Yao, Y., Miao, C., Zheng, Y.M., Liu, S.L., Guo, F., Geng, Y., Qiao, W., and Liang, C. (2014). Identification of an endocytic signal essential for the antiviral action of IFITM3. Cell Microbiol. *16*, 1080–1093. https://doi.org/10.1111/cmi.12262.

Jiang, D., Weidner, J.M., Qing, M., Pan, X.B., Guo, H., Xu, C., Zhang, X., Birk, A., Chang, J., Shi, P.Y., et al. (2010). Identification of five interferon-induced cellular proteins that inhibit west nile virus and dengue virus infections. J. Virol. *84*, 8332–8341. https://doi.org/10.1128/JVI.02199-09.

Jurado, K.A., Yockey, L.J., Wong, P.W., Lee, S., Huttner, A.J., and Iwasaki, A. (2018). Antiviral CD8 T cells induce Zika-virus-associated paralysis in mice. Nat. Microbiol. *3*, 141–147. https://doi.org/10.1038/s41564-017-0060-z.

Kalia, M., Khasa, R., Sharma, M., Nain, M., and Vrati, S. (2013). Japanese encephalitis virus infects neuronal cells through a clathrin-independent endocytic mechanism. J. Virol. *87*, 148–162. https://doi.org/10.1128/JVI.01399-12.

Kendra, J.A., de la Fuente, C., Brahms, A., Woodson, C., Bell, T.M., Chen, B., Khan, Y.A., Jacobs, J.L., Kehn-Hall, K., and Dinman, J.D. (2017). Ablation of programmed -1 ribosomal frameshifting in Venezuelan equine encephalitis

virus results in attenuated neuropathogenicity. J. Virol. *91*, e01766-16. https://doi.org/10.1128/JVI.01766-16.

Kraus, J., Ling, A.K., Hamm, S., Voigt, K., Oschmann, P., and Engelhardt, B. (2004). Interferon-beta stabilizes barrier characteristics of brain endothelial cells in vitro. Ann. Neurol. *56*, 192–205. https://doi.org/10.1002/ana.20161.

Kumar, M., Belcaid, M., and Nerurkar, V.R. (2016). Identification of host genes leading to West Nile virus encephalitis in mice brain using RNA-seq analysis. Sci. Rep. *6*, 26350. https://doi.org/10.1038/srep26350.

Lafaille, F.G., Harschnitz, O., Lee, Y.S., Zhang, P., Hasek, M.L., Kerner, G., Itan, Y., Ewaleifoh, O., Rapaport, F., Carlile, T.M., et al. (2019). Human SNORA31 variations impair cortical neuron-intrinsic immunity to HSV-1 and underlie herpes simplex encephalitis. Nat. Med. *25*, 1873–1884. https://doi.org/10.1038/s41591-019-0672-3.

Lafaille, F.G., Pessach, I.M., Zhang, S.Y., Ciancanelli, M.J., Herman, M., Abhyankar, A., Ying, S.W., Keros, S., Goldstein, P.A., Mostoslavsky, G., et al. (2012). Impaired intrinsic immunity to HSV-1 in human iPSC-derived TLR3-deficient CNS cells. Nature *491*, 769–773. https://doi.org/10.1038/nature11583.

Lauschke, K., Frederiksen, L., and Hall, V.J. (2017). Paving the way toward complex blood-brain barrier models using pluripotent stem cells. Stem Cells Dev. *26*, 857–874. https://doi.org/10.1089/scd.2017.0003.

Lazear, H.M., Daniels, B.P., Pinto, A.K., Huang, A.C., Vick, S.C., Doyle, S.E., Gale, M., Jr., Klein, R.S., and Diamond, M.S. (2015). Interferon-lambda restricts West Nile virus neuroinvasion by tightening the blood-brain barrier. Sci. Transl. Med. *7*, 284ra259. https://doi.org/10.1126/scitranslmed.aaa4304.

Li, C., Du, S., Tian, M., Wang, Y., Bai, J., Tan, P., Liu, W., Yin, R., Wang, M., Jiang, Y., et al. (2018). The host restriction factor interferon-inducible transmembrane protein 3 inhibits vaccinia virus infection. Front. Immunol. *9*, 228. https://doi.org/10.3389/fimmu.2018.00228.

Li, K., Markosyan, R.M., Zheng, Y.M., Golfetto, O., Bungart, B., Li, M., Ding, S., He, Y., Liang, C., Lee, J.C., et al. (2013). IFITM proteins restrict viral membrane hemifusion. PLoS Pathog. *9*, e1003124. https://doi.org/10.1371/journal.ppat.1003124.

Li, L., Jose, J., Xiang, Y., Kuhn, R.J., and Rossmann, M.G. (2010). Structural changes of envelope proteins during alphavirus fusion. Nature *468*, 705–708. https://doi.org/10.1038/nature09546.

Liao, Y., Goraya, M.U., Yuan, X., Zhang, B., Chiu, S.H., and Chen, J.L. (2019). Functional involvement of interferon-inducible transmembrane proteins in antiviral immunity. Front. Microbiol. *10*, 1097. https://doi.org/10.3389/fmicb.2019.01097.

Lippmann, E.S., Al-Ahmad, A., Azarin, S.M., Palecek, S.P., and Shusta, E.V. (2014). A retinoic acid-enhanced, multicellular human blood-brain barrier model derived from stem cell sources. Sci. Rep. *4*, 4160. https://doi.org/10.1038/srep04160.

Lippmann, E.S., Azarin, S.M., Kay, J.E., Nessler, R.A., Wilson, H.K., Al-Ahmad, A., Palecek, S.P., and Shusta, E.V. (2012). Derivation of blood-brain barrier endothelial cells from human pluripotent stem cells. Nat. Biotechnol. *30*, 783–791. https://doi.org/10.1038/nbt.2247.

Lippmann, E.S., Azarin, S.M., Palecek, S.P., and Shusta, E.V. (2020). Commentary on human pluripotent stem cell-based blood-brain barrier models. Fluids Barriers CNS *17*, 64. https://doi.org/10.1186/s12987-020-00222-3.

Lou, E., Fujisawa, S., Morozov, A., Barlas, A., Romin, Y., Dogan, Y., Gholami, S., Moreira, A.L., Manova-Todorova, K., and Moore, M.A.S. (2012). Tunneling nanotubes provide a unique conduit for intercellular transfer of cellular contents in human malignant pleural mesothelioma. PLoS One *7*, e33093. https://doi.org/10.1371/journal.pone.0033093.

Lu, T.M., Houghton, S., Magdeldin, T., Duran, J.G.B., Minotti, A.P., Snead, A., Sproul, A., Nguyen, D.H.T., Xiang, J., Fine, H.A., et al. (2021). Pluripotent stem cell-derived epithelium misidentified as brain microvascular endothelium requires ETS factors to acquire vascular fate. Proc. Natl. Acad. Sci. U S A *118*. https://doi.org/10.1073/pnas.2016950118.

Lustig, S., Halevy, M., Ben-Nathan, D., and Akov, Y. (1992). A novel variant of Sindbis virus is both neurovirulent and neuroinvasive in adult mice. Arch. Virol. *122*, 237–248. https://doi.org/10.1007/BF01317186.

Ma, W., Li, S., Ma, S., Jia, L., Zhang, F., Zhang, Y., Zhang, J., Wong, G., Zhang, S., Lu, X., et al. (2017). Zika virus causes testis damage and leads to male infertility in mice. Cell *168*, 542. https://doi.org/10.1016/j.cell.2017.01.009.

Matusali, G., Houzet, L., Satie, A.P., Mahe, D., Aubry, F., Couderc, T., Frouard, J., Bourgeau, S., Bensalah, K., Lavoue, S., et al. (2018). Zika virus infects human testicular tissue and germ cells. J. Clin. Invest. *128*, 4697–4710. https://doi.org/10.1172/JCI121735.

Mesci, P., Macia, A., LaRock, C.N., Tejwani, L., Fernandes, I.R., Suarez, N.A., de A Zanotto, P.M., Beltrao-Braga, P.C.B., Nizet, V., and Muotri, A.R. (2018). Modeling neuro-immune interactions during Zika virus infection. Hum. Mol. Genet. *27*, 41–52. https://doi.org/10.1093/hmg/ddx382.

Mladinich, M.C., Schwedes, J., and Mackow, E.R. (2017). Zika virus persistently infects and is basolaterally released from primary human brain microvascular endothelial cells. mBio *8*, e00952-17. https://doi.org/10.1128/mBio.00952-17.

Mruk, D.D., and Cheng, C.Y. (2015). The mammalian blood-testis barrier: its biology and regulation. Endocr. Rev. *36*, 564–591. https://doi.org/10.1210/er.2014-1101.

Muffat, J., Li, Y., Omer, A., Durbin, A., Bosch, I., Bakiasi, G., Richards, E., Meyer, A., Gehrke, L., and Jaenisch, R. (2018). Human induced pluripotent stem cell-derived glial cells and neural progenitors display divergent responses to Zika and dengue infections. Proc. Natl. Acad. Sci. U S A *115*, 7117–7122. https://doi.org/10.1073/pnas.1719266115.

Munoz-Moreno, R., Cuesta-Geijo, M.A., Martinez-Romero, C., Barrado-Gil, L., Galindo, I., Garcia-Sastre, A., and Alonso, C. (2016). Antiviral role of IFITM proteins in African swine fever virus infection. PLoS One *11*, e0154366. https://doi.org/10.1371/journal.pone.0154366.

Narayana, S.K., Helbig, K.J., McCartney, E.M., Eyre, N.S., Bull, R.A., Eltahla, A., Lloyd, A.R., and Beard, M.R. (2015). The interferon-induced transmembrane proteins, IFITM1, IFITM2, and IFITM3 inhibit hepatitis C virus entry. J. Biol. Chem. *290*, 25946–25959. https://doi.org/10.1074/jbc.M115.657346.

Neal, E.H., Marinelli, N.A., Shi, Y., McClatchey, P.M., Balotin, K.M., Gullett, D.R., Hagerla, K.A., Bowman, A.B., Ess, K.C., Wikswo, J.P., and Lippmann, E.S. (2019). A simplified, fully defined differentiation scheme for producing blood-brain barrier endothelial cells from human iPSCs. Stem Cell Rep. *12*, 1380–1388. https://doi.org/10.1016/j.stemcr.2019.05.008.

Ohshima, M., Kamei, S., Fushimi, H., Mima, S., Yamada, T., and Yamamoto, T. (2019). Prediction of drug permeability using in vitro blood-brain barrier models with human induced pluripotent stem cell-derived brain microvascular endothelial cells. BioResearch Open Access *8*, 200–209. https://doi.org/10.1089/biores.2019.0026.

Pan, P., Li, G., Shen, M., Yu, Z., Ge, W., Lao, Z., Fan, Y., Chen, K., Ding, Z., Wang, W., et al. (2021). DENV NS1 and MMP-9 cooperate to induce vascular leakage by altering endothelial cell adhesion and tight junction. PLoS Pathog. *17*, e1008603. https://doi.org/10.1371/journal.ppat.1008603.

Paradis, A., Leblanc, D., and Dumais, N. (2016). Optimization of an in vitro human blood-brain barrier model: application to blood monocyte transmigration assays. MethodsX *3*, 25–34. https://doi.org/10.1016/j.mex.2015.11.009.

Perreira, J.M., Chin, C.R., Feeley, E.M., and Brass, A.L. (2013). IFITMs restrict the replication of multiple pathogenic viruses. J. Mol. Biol. *425*, 4937–4955. https://doi.org/10.1016/j.jmb.2013.09.024.

Pierson, T.C., and Diamond, M.S. (2018). The emergence of Zika virus and its new clinical syndromes. Nature *560*, 573–581. https://doi.org/10.1038/s41586-018-0446-y.

Poddar, S., Hyde, J.L., Gorman, M.J., Farzan, M., and Diamond, M.S. (2016). The interferon-stimulated gene IFITM3 restricts infection and pathogenesis of arthritogenic and encephalitic alphaviruses. J. Virol. *90*, 8780–8794. https://doi.org/10.1128/JVI.00655-16.

Popson, S.A., Ziegler, M.E., Chen, X., Holderfield, M.T., Shaaban, C.I., Fong, A.H., Welch-Reardon, K.M., Papkoff, J., and Hughes, C.C. (2014).

Interferon-induced transmembrane protein 1 regulates endothelial lumen formation during angiogenesis. Arterioscler. Thromb. Vasc. Biol. *34*, 1011–1019. https://doi.org/10.1161/ATVBAHA.114.303352.

Puerta-Guardo, H., Glasner, D.R., Espinosa, D.A., Biering, S.B., Patana, M., Ratnasiri, K., Wang, C., Beatty, P.R., and Harris, E. (2019). Flavivirus NS1 triggers tissue-specific vascular endothelial dysfunction reflecting disease tropism. Cell Rep. *26*, 1598–1613.e8. https://doi.org/10.1016/j.celrep.2019.01.036.

Qian, T., Maguire, S.E., Canfield, S.G., Bao, X., Olson, W.R., Shusta, E.V., and Palecek, S.P. (2017). Directed differentiation of human pluripotent stem cells to blood-brain barrier endothelial cells. Sci. Adv. *3*, e1701679. https://doi.org/10.1126/sciadv.1701679.

Qian, X., Jacob, F., Song, M.M., Nguyen, H.N., Song, H., and Ming, G.L. (2018). Generation of human brain region-specific organoids using a miniaturized spinning bioreactor. Nat. Protoc. *13*, 565–580. https://doi.org/10.1038/nprot.2017.152.

Qian, X., Nguyen, H.N., Song, M.M., Hadiono, C., Ogden, S.C., Hammack, C., Yao, B., Hamersky, G.R., Jacob, F., Zhong, C., et al. (2016). Brain-region-specific organoids using mini-bioreactors for modeling ZIKV exposure. Cell *165*, 1238–1254. https://doi.org/10.1016/j.cell.2016.04.032.

Rice, C.M., Levis, R., Strauss, J.H., and Huang, H.V. (1987). Production of infectious RNA transcripts from Sindbis virus cDNA clones: mapping of lethal mutations, rescue of a temperature-sensitive marker, and in vitro mutagenesis to generate defined mutants. J. Virol. *61*, 3809–3819. https://doi.org/10.1128/JVI.61.12.3809-3819.1987.

Roach, T., and Alcendor, D.J. (2017). Zika virus infection of cellular components of the blood-retinal barriers: implications for viral associated congenital ocular disease. J. Neuroinflammation *14*, 43. https://doi.org/10.1186/s12974-017-0824-7.

Salimi, H., Cain, M.D., Jiang, X., Roth, R.A., Beatty, W.L., Sun, C., Klimstra, W.B., Hou, J., and Klein, R.S. (2020). Encephalitic alphaviruses exploit caveola-mediated transcytosis at the blood-brain barrier for central nervous system entry. mBio *11*, e02731-19. https://doi.org/10.1128/mBio.02731-19.

Salinas, S., Erkilic, N., Damodar, K., Moles, J.P., Fournier-Wirth, C., Van de Perre, P., Kalatzis, V., and Simonin, Y. (2017). Zika virus efficiently replicates in human retinal epithelium and disturbs its permeability. J. Virol. *91*, e02144-16. https://doi.org/10.1128/JVI.02144-16.

Sanjana, N.E., Shalem, O., and Zhang, F. (2014). Improved vectors and genome-wide libraries for CRISPR screening. Nat. Methods *11*, 783–784. https://doi.org/10.1038/nmeth.3047.

Sato, T., Stange, D.E., Ferrante, M., Vries, R.G., Van Es, J.H., Van den Brink, S., Van Houdt, W.J., Pronk, A., Van Gorp, J., Siersema, P.D., and Clevers, H. (2011). Long-term expansion of epithelial organoids from human colon, adenoma, adenocarcinoma, and Barrett's epithelium. Gastroenterology *141*, 1762–1772. https://doi.org/10.1053/j.gastro.2011.07.050.

Savidis, G., Perreira, J.M., Portmann, J.M., Meraner, P., Guo, Z., Green, S., and Brass, A.L. (2016). The IFITMs inhibit Zika virus replication. Cell Rep. *15*, 2323–2330. https://doi.org/10.1016/j.celrep.2016.05.074.

Schoggins, J.W., Wilson, S.J., Panis, M., Murphy, M.Y., Jones, C.T., Bieniasz, P., and Rice, C.M. (2011). A diverse range of gene products are effectors of the type I interferon antiviral response. Nature *472*, 481–485. https://doi.org/10.1038/nature09907.

Siemann, D.N., Strange, D.P., Maharaj, P.N., Shi, P.Y., and Verma, S. (2017). Zika virus infects human Sertoli cells and modulates the integrity of the in vitro blood-testis barrier model. J. Virol. *91*. https://doi.org/10.1128/JVI.00623-17.

Singh, P.K., Guest, J.M., Kanwar, M., Boss, J., Gao, N., Juzych, M.S., Abrams, G.W., Yu, F.S., and Kumar, A. (2017). Zika virus infects cells lining the blood-retinal barrier and causes chorioretinal atrophy in mouse eyes. JCI Insight *2*, e92340. https://doi.org/10.1172/jci.insight.92340.

Singh, P.K., Khatri, I., Jha, A., Pretto, C.D., Spindler, K.R., Arumugaswami, V., Giri, S., Kumar, A., and Bhasin, M.K. (2018). Determination of system level alterations in host transcriptome due to Zika virus (ZIKV) Infection in retinal pigment epithelium. Sci. Rep. *8*, 11209. https://doi.org/10.1038/s41598-018-29329-2.

Spence, J.S., He, R., Hoffmann, H.H., Das, T., Thinon, E., Rice, C.M., Peng, T., Chandran, K., and Hang, H.C. (2019). IFITM3 directly engages and shuttles incoming virus particles to lysosomes. Nat. Chem. Biol. *15*, 259–268. https://doi.org/10.1038/s41589-018-0213-2.

Suddala, K.C., Lee, C.C., Meraner, P., Marin, M., Markosyan, R.M., Desai, T.M., Cohen, F.S., Brass, A.L., and Melikyan, G.B. (2019). Interferon-induced transmembrane protein 3 blocks fusion of sensitive but not resistant viruses by partitioning into virus-carrying endosomes. PLoS Pathog. *15*, e1007532. https://doi.org/10.1371/journal.ppat.1007532.

Sumpter, R., Jr., Loo, Y.M., Foy, E., Li, K., Yoneyama, M., Fujita, T., Lemon, S.M., and Gale, M., Jr. (2005). Regulating intracellular antiviral defense and permissiveness to hepatitis C virus RNA replication through a cellular RNA helicase, RIG-I. J. Virol. *79*, 2689–2699. https://doi.org/10.1128/JVI.79.5.2689-2699.2005.

Sutarjono, B. (2019). Can we better understand how Zika leads to microcephaly? A systematic review of the effects of the Zika virus on human brain organoids. J. Infect. Dis. *219*, 734–745. https://doi.org/10.1093/infdis/jiy572.

Tamhankar, M., and Patterson, J.L. (2019). Directional entry and release of Zika virus from polarized epithelial cells. Virol. J. *16*, 99. https://doi.org/10.1186/s12985-019-1200-2.

Tang, H., Hammack, C., Ogden, S.C., Wen, Z., Qian, X., Li, Y., Yao, B., Shin, J., Zhang, F., Lee, E.M., et al. (2016). Zika virus infects human cortical neural progenitors and attenuates their growth. Cell Stem Cell *18*, 587–590. https://doi.org/10.1016/j.stem.2016.02.016.

Uraki, R., Hwang, J., Jurado, K.A., Householder, S., Yockey, L.J., Hastings, A.K., Homer, R.J., Iwasaki, A., and Fikrig, E. (2017). Zika virus causes testicular atrophy. Sci. Adv. *3*, e1602899. https://doi.org/10.1126/sciadv.1602899.

Verma, S., Lo, Y., Chapagain, M., Lum, S., Kumar, M., Gurjav, U., Luo, H., Nakatsuka, A., and Nerurkar, V.R. (2009). West Nile virus infection modulates human brain microvascular endothelial cells tight junction proteins and cell adhesion molecules: transmigration across the in vitro blood-brain barrier. Virology *385*, 425–433. https://doi.org/10.1016/j.virol.2008.11.047.

Voss, J.E., Vaney, M.C., Duquerroy, S., Vonrhein, C., Girard-Blanc, C., Crublet, E., Thompson, A., Bricogne, G., and Rey, F.A. (2010). Glycoprotein organization of Chikungunya virus particles revealed by X-ray crystallography. Nature *468*, 709–712. https://doi.org/10.1038/nature09555.

Wakim, L.M., Gupta, N., Mintern, J.D., and Villadangos, J.A. (2013). Enhanced survival of lung tissue-resident memory CD8(+) T cells during infection with influenza virus due to selective expression of IFITM3. Nat. Immunol. *14*, 238–245. https://doi.org/10.1038/ni.2525.

Weksler, B.B., Subileau, E.A., Perriere, N., Charneau, P., Holloway, K., Leveque, M., Tricoire-Leignel, H., Nicotra, A., Bourdoulous, S., Turowski, P., et al. (2005). Blood-brain barrier-specific properties of a human adult brain endothelial cell line. FASEB J. *19*, 1872–1874. https://doi.org/10.1096/fj.04-3458fje.

Wen, Z., Nguyen, H.N., Guo, Z., Lalli, M.A., Wang, X., Su, Y., Kim, N.S., Yoon, K.J., Shin, J., Zhang, C., et al. (2014). Synaptic dysregulation in a human iPS cell model of mental disorders. Nature *515*, 414–418. https://doi.org/10.1038/nature13716.

Wessel, A.W., Dowd, K.A., Biering, S.B., Zhang, P., Edeling, M.A., Nelson, C.A., Funk, K.E., DeMaso, C.R., Klein, R.S., Smith, J.L., Cao, T.M., Kuhn, R.J., Fremont, D.H., Harris, E., Pierson, T.C., and Diamond, M.S. (2021). Levels of circulating NS1 impact West Nile virus spread to the brain. J. Virol. *95*, e0084421. https://doi.org/10.1128/JVI.00844-21.

Wilkins, C., Woodward, J., Lau, D.T.Y., Barnes, A., Joyce, M., McFarlane, N., McKeating, J.A., Tyrrell, D.L., and Gale, M., Jr. (2013). IFITM1 is a tight junction protein that inhibits hepatitis C virus entry. Hepatology *57*, 461–469. https://doi.org/10.1002/hep.26066.

Wu, X., Dao Thi, V.L., Huang, Y., Billerbeck, E., Saha, D., Hoffmann, H.H., Wang, Y., Silva, L.A.V., Sarbanes, S., Sun, T., et al. (2018). Intrinsic immunity

shapes viral resistance of stem cells. Cell *172*, 423–438.e25. https://doi.org/10.1016/j.cell.2017.11.018.

Wu, X., Robotham, J.M., Lee, E., Dalton, S., Kneteman, N.M., Gilbert, D.M., and Tang, H. (2012). Productive hepatitis C virus infection of stem cell-derived hepatocytes reveals a critical transition to viral permissiveness during differentiation. Plos Pathog. *8*, e1002617. https://doi.org/10.1371/journal.ppat.1002617.

Xu, J., Qian, P., Wu, Q., Liu, S., Fan, W., Zhang, K., Wang, R., Zhang, H., Chen, H., and Li, X. (2014). Swine interferon-induced transmembrane protein, sIFITM3, inhibits foot-and-mouth disease virus infection in vitro and in vivo. Antivir. Res. *109*, 22–29. https://doi.org/10.1016/j.antiviral.2014.06.008.

Zhao, X., Li, J., Winkler, C.A., An, P., and Guo, J.T. (2019). IFITM genes, variants, and their roles in the control and pathogenesis of viral infections. Front. Microbiol. *9*, 3228. https://doi.org/10.3389/fmicb.2018.03228.

Zhu, R., Wang, J., Lei, X.Y., Gui, J.F., and Zhang, Q.Y. (2013). Evidence for Paralichthys olivaceus IFITM1 antiviral effect by impeding viral entry into target cells. Fish Shellfish Immunol. *35*, 918–926. https://doi.org/10.1016/j.fsi.2013.07.002.

Zimmer, B., Ewaleifoh, O., Harschnitz, O., Lee, Y.S., Peneau, C., McAlpine, J.L., Liu, B., Tchieu, J., Steinbeck, J.A., Lafaille, F., et al. (2018). Human iPSC-derived trigeminal neurons lack constitutive TLR3-dependent immunity that protects cortical neurons from HSV-1 infection. Proc. Natl. Acad. Sci. U S A *115*, E8775–E8782. https://doi.org/10.1073/pnas.1809853115.

STAR★METHODS

KEY RESOURCES TABLE

REAGENT or RESOURCE	SOURCE	IDENTIFIER
Antibodies		
Mouse monoclonal anti-IFITM1 1:10000	Proteintech	Cat#60074-1-Ig; RRID:AB_530619
Mouse monoclonal anti-IFITM2 1:2000	Proteintech	Cat#66137-1-Ig; RRID:AB_2881536
Rabbit monoclonal anti-IFITM3 1:5000	Cell Signaling Technology	Cat#D8E8G; RRID:AB_2799561
Rabbit polyclonal anti-GAPDH 1:50000	GeneTex	Cat#GTX100118; RRID:AB_1080976
Mouse monoclonal anti-Ku80 1:3000	Abcam	Cat#ab119935; RRID:AB_10899161
Mouse monoclonal anti-Zika Envelope NS1 2000	BioFront Technologies	Cat#BF-1176-46-1mg
Mouse monoclonal anti-dsRNA antibody, clone J2	Sigma-Aldrich	Cat#MABE1134; RRID:AB_2819101
Rabbit polyclonal anti-ZO-1	ThermoFisher	Cat#40-2200; RRID:AB_2533456
Rabbit polyclonal anti-S100B	ThermoFisher	Cat#PA5-87474; RRID:AB_2804180
Rabbit polyclonal anti-GLUT1	Abcam	Cat#ab15309; RRID:AB_301844
Goat polyclonal anti-ZO-1	Novus	Cat#NBP1-46111; RRID:AB_10009353
Mouse monoclonal anti-P-glycoprotein	ThermoFisher	Cat#MA5-13854; RRID:AB_10979045
Rabbit polyclonal anti-Claudin 5	ThermoFisher	Cat#34-1600; RRID:AB_86930
Rabbit polyclonal anti-CD31	Abcam	Cat#ab28364; RRID:AB_726362
Goat Anti-Rabbit IgG (H+L) secondary antibody, HRP conjugate	Abcam	Cat#Ab6721; RRID:AB_955447
Goat Anti-Mouse IgG (H+L) secondary antibody, HRP conjugate	Abcam	Cat#Ab6789; RRID:AB_955439
Goat Anti-Rabbit IgG (H+L) secondary antibody, Cy3 conjugate	Invitrogen	Cat#A10521; RRID:AB_1500665
Goat Anti-Mouse IgG (H+L) secondary antibody, Cy3 conjugate	Invitrogen	Cat#A10520; RRID:AB_2534029
Goat Anti-Rabbit IgG (whole molecule)-FITC	Sigma-Aldrich	Cat#F0382; RRID:AB_259384
Goat Anti-Mouse IgG (whole molecule)-FITC	Sigma-Aldrich	Cat#F0257; RRID:AB_259378
Bacterial and virus strains		
Dengue Virus (Type 1, strain Hawaii)	BEI resources	Cat#NR-82
Dengue Virus (Type 3, strain MK-594-87)	BEI resources	Cat#NR-3799
Dengue Virus Type 4, H241	BEI resources	Cat#NR-86
Dengue Virus Type 2, 16681	Laboratory of Qianjun Li	N/A
Zika Virus (strain PRVABC59)	ATCC	Cat#VR-1843
Zika Virus (strain MR766)	ZeptoMetrix	Cat#0810521CF
Yellow Fever Virus (strain YFV-17D)	Laboratory of Qianjun Li	N/A
West Nile Virus, WNV Eg101	Hilary Koprowski, Wistar Institute	N/A
West Nile Virus, WNV NY99	Robert Tesh, UTMB, Galveston TX	N/A
West Nile Virus, WNV MAD78	Robert Tesh, UTMB, Galveston TX	N/A
Powassan Virus, POWV LB strain	BEI resources	Cat#NR-51181
Usutu Virus, USUV	BEI resources	Cat#NR-51184
Japanese Encephalitis Virus, JEV Nakayama strain	BEI resources	Cat#NR-90
SVN-GFP	Laboratory of Charles M. Rice	Dubuisson et al., 1997
R47-GFP	Laboratory of Charles M. Rice	Dubuisson et al., 1997
SVN	Laboratory of Charles M. Rice	Dubuisson et al., 1997; Lustig et al., 1992
SVNI	Laboratory of Charles M. Rice	Dubuisson et al., 1997; Lustig et al., 1992

(*Continued on next page*)

Continued

REAGENT or RESOURCE	SOURCE	IDENTIFIER
Chemicals, peptides, and recombinant proteins		
Vascular cell basal medium	ATCC	Cat#PCS-100-030
Sertoli cell medium complete	ScienCell	Cat#4521
Microvascular endothelial cell growth kit-VEGF	ATCC	Cat#PCS-110-041
Complete classic medium with serum and CultureBoost	Cell systems	Cat#4Z0-500
Attachment Factor	Cell systems	Cat#4Z0-210
Dulbecco's Modified Eagle Medium/Nutrient Mixture F-12. DMEM: F12	Invitrogen	Cat#11330032
Corning® Matrigel® Growth Factor Reduced (GFR) Basement Membrane Matrix	Corning	Cat#354230
Astrocyte medium complete	ScienCell	Cat#1801
Neurobasal medium	GIBCO	Cat#21103049
Poly-L-Lysine	ScienCell	Cat#0403
Poly-D-lysine hydrobromide	Sigma-Aldrich	Cat#P6407
Trypsin/EDTA Solution	Gibco	Cat#R001100
mTESR1	STEMCELL Technologies	Cat#85857
Knockout Serum Replacer	Gibco	Cat#10828028
MEM nonessential amino acids	Gibco	Cat#11140050
L-glutamine	Gibco	Cat#25030149
β-mercaptoethanol	Gibco	Cat#31350010
human basic fibroblast growth factor (bFGF)	STEMCELL Technologies	Cat#78003
Retinoic Acid (RA)	Sigma-Aldrich	Cat#R2625
human Endothelial Serum-Free Media	Gibco	Cat#11111044
Antibiotic-Antimycotic: Streptomycin, Amphotericin B and Penicillin	Gibco	Cat#15240062
Normal Goat Serum	ThermoFisher Scientific	Cat#10000C
Fibronectin from human plasma	Sigma-Aldrich	Cat#F1056
Collagen type I, Rat tail	Sigma-Aldrich	Cat#08-115
N2 Supplement	GIBCO	Cat#17502048
B27 Supplements	GIBCO	Cat#17504044
Recombinant Human VEGF	R&D system	Cat#293-VE-010/CF
Recombinant Human CCL2/MCP-1 Protein	Novus	Cat#279-MC-010
Recombinant Human TNF-alpha Protein	Novus	Cat#NBP2-35076-10ug
Ascorbic Acid	Sigma	Cat#1043003
StemPro™ Accutase™ Cell Dissociation Reagent	Gibco	Cat#A1110501
ROCK Inhibitor Y-27632	STEMCELL Technologies	Cat#72304
Dimethyl Sulfoxide (DMSO)	Sigma-Aldrich	Cat#D8418
Paraformaldehyde	Sigma-Aldrich	Cat#158127
Methyl cellulose	Sigma-Aldrich	Cat#M0512
Triton-X-100	Sigma-Aldrich	Cat#T8787
Bovine serum albumin (BSA)	Sigma-Aldrich	Cat#A7906
Tween-20	Fisher BioReagents	Cat#BP337500
Agarose, molecular biology grade	Fisher BioReagents	Cat#BP16525
Lipofectamine 2000	ThermoFisher	Cat#11668019
Polybrene	Santa Cruz animal health	Cat#sc-134220
VECTASHIELD mounting medium for fluorescence	Vector Laboratories	Cat#H-1200; RRID:AB_2336790
ProLong Gold antifade mountant	ThermoFisher	Cat# P10144
Hoechst 33258, Pentahydrate	ThermoFisher	Cat# H1398
DAB substrate kit	Vector Laboratories	Cat#SK-4100; RRID:AB_2336382

(*Continued on next page*)

Continued

REAGENT or RESOURCE	SOURCE	IDENTIFIER
Immobilon Western chemiluminescent HRP substrate	Millipore	Cat#WBKLS0500
Sp6 RNA polymerase	NEB	Cat#M0207S
SacI-HF	NEB	Cat#R3156S
ClaI	NEB	Cat#R0197S
AatII	NEB	Cat#R0117S
BsHII	NEB	Cat#R0199S
Human brain microvascular endothelial cell lysate	ScienCell	Cat#1006
Sodium Citrate Dihydrate	Fisher Scientific	Cat#BP327-500
Brain Cerebral Cortex Tissue Slides (Adult Normal)	Novus Biologicals	Cat#NBP2-77755
Rhodamine 123	Sigma	Cat#R8004
Cyclosporin A	Sigma	Cat#SML1018
Critical commercial assays		
Human cytokine array/chemokine array 65-plex panel	Eve Technologies	Cat#HD65
QuikChange lightning site-directed mutagenesis kit	Agilent	Cat#210519
Zero Blunt PCR Cloning Kit	ThermoFisher	Cat# 450245
Superscript III First-Strand Synthesis System	Life Technologies	Cat#18080051
RNeasy plus mini kit	QIAGEN	Cat#74134
Experimental models: Cell lines		
hESCs (H9)	WiCell – University Wisconsin-Madison	WA09; RRID:CVCL_9773
iPS(IMR90) clone #4	WiCell – University Wisconsin-Madison	iPS(IMR90)-4; RRID:CVCL_C437
iPSC DF19-9-11T.H	WiCell – University Wisconsin-Madison	iPS DF19-9-11T.H; RRID:CVCL_K054
Forebrain organoids	Laboratory of Guo-Li Ming	Qian et al., 2016, 2018
Human neural progenitor cells (hNPCs)	Laboratory of Zhexing Wen	Wen et al., 2014
THP-1	ATCC	Cat#TIB-202; RRID:CVCL_0006
HEK293	ATCC	Cat#CRL-1573; RRID:CVCL_0045
Vero	ATCC	Cat#CCL-81; RRID:CVCL_0059
SNB-19	Laboratory of David Meckes	NCI-60 Human Cancer Cell Line Screen
Huh7.5	Laboratory of Charles M. Rice	Blight et al., 2002
C6/36	ATCC	Cat# CRL-1660
hCMEC/D3	Laboratory of Ren Sun	Weksler et al., 2005
Primary Umbilical Vein Endothelial Cells (HUVEC), passage 2 - 6	ATCC	Cat#PCS-100-013
Primary human Sertoli cells, passage 2 - 6	ScienCell	Cat#4520
Primary human retinal microvascular endothelial cells (RMEC), passage 4 - 6	Cell systems	Cat#ACBRI 181
Primary human retinal epithelial (RPE) cells, passage 2 - 4	Lonza	Cat#00194987
Human Astrocytes-midbrain	ScienCell	Cat#1850
Human Primary Astrocytes	ScienCell	Cat#1800
Oligonucleotides		
Forward primer for cloning IFITM1 (5′-3′): TATGGATCCA TGCACAAGGAGGAACATGA	This paper	N/A
Reverse primer for cloning IFITM1 (5′-3′): AAGGAATTCCT AGTAACCCCGTTTTTCCT	This paper	N/A
gRNA-IFITM1: TGATCACGGTGGACCTTGGA	This paper	N/A
gRNA-IFITM123: TCTAGGGACAGGAAGATGGT	This paper	N/A

(*Continued on next page*)

Continued

REAGENT or RESOURCE	SOURCE	IDENTIFIER
Primers for Alphaviruses mutagenesis, see Table S1	This paper	N/A
Primers for RT-qPCR, see Table S2	This paper	N/A
Recombinant DNA		
pUltra	Lou et al., 2012	Addgene plasmid #24129
lentiCRISPR v2	Sanjana et al., 2014	Addgene plasmid #52961
Software and algorithms		
ImageJ (Fiji)	NIH	ImageJ, RRID:SCR_003070
Adobe Photoshop (CC)	Adobe	Adobe Photoshop, RRID: SCR_014199
GraphPad Prism	GraphPad	GraphPad Prism, RRID: SCR_002798
Flowjo	https://flowjo.com	Tre Star; FlowJo RRID: SCR_008520
Other		
4-chip disposable hemocytometer	Bulldog Bio	Cat#DHC-N404
Corning® Transwell® polycarbonate membrane cell culture inserts	Corning	Cat#CLS3401
Corning® Transwell® polyester membrane cell culture inserts	Corning	Cat#CLS3460
Epithelial Volt/Ohm (TEER) Meter (EVOM2)	World Precision Instruments	Cat#EVOM2
SpinΩ 12-well Spinning Bioreactor	Qian et al., 2016, 2018	N/A
Cuvettes Plus™ Electroporation Cuvettes, BTX™, 2mm gap, 400 ul	BTX	Cat#58017-895

RESOURCE AVAILABILITY

Lead contact

Requests for resources and reagents should be directed to the lead contact, Hengli Tang (tang@bio.fsu.edu).

Materials availability

All unique reagents generated in this study are available from the lead contact with completed Material Transfer Agreements.

Data and code availability

The datasets supporting the current study are available from the lead contact on request.

This paper does not report original code.

Any additional information required to reanalyze the data reported in this paper in available from the lead contact upon request.

EXPERIMENTAL MODEL AND SUBJECT DETAILS

Cell lines

Human ESC and iPSC lines

Human embryonic stem cell line H9 (WA09; sex: female), human induced pluripotent stem cell lines iPS (IMR90)-4 (sex: female) and iPS DF19-9-11T.H (sex: male) were thawed on Matrigel™ coated flasks and cultured in stem cell media (mTESR1). For all the experiments in this study, hES or iPSCs were used between passages 38 and 42.

Human primary cells

Primary human umbilical vein endothelial cell (HUVECs) were cultured in vascular cell basal medium supplemented with endothelial cell growth kit-VEGF at 37°C and 5% CO_2. hCMEC/D3 were cultured in Collagen type I (5 μg/cm^2) coated culture vessels using EndoGRO™-MV complete media kit supplemented with 1 ng/mL basic fibroblast growth factor (bFGF). Primary human Sertoli cells were cultured in Poly-L-Lysine (2 μg/cm^2) coated culture vessels using supplemented Sertoli cell medium according to the provider's instruction at 37°C and 5% CO_2. Primary human retinal microvascular endothelial cells (RMECs) were cultured in Attachment Factor™-coated culture vessels and incubated with complete classic medium supplemented with serum and CultureBoost™ at 37°C and 5% CO_2. Primary human retinal epithelial cells (RPEs) were maintained with RtEGM™ retinal pigment epithelial cell growth medium Bulletkit™ according to the manufacturer's protocol and cultured at 37°C and 5% CO_2. Primary human astrocytes were

cultured in Poly-D-lysine (2 μg/cm^2) coated culture vessels using supplemented astrocyte media according to the provider's instructions at 37°C and 5% CO_2.

Other cell lines

Aedes albopictus C6/36 cells, used for propagation of the viruses, were cultured in Eagle's minimum essential medium (EMEM) supplemented with 10% FBS and incubated at 28°C in 5% CO_2. The human glioblastoma SNB-19 cells were grown in RPMI 1640 medium supplemented with 10% fetal bovine serum (FBS) at 37°C and 5% CO_2. Huh7.5, Vero and HEK-293T cells were maintained in Dulbecco's modified Eagle's medium (DMEM) supplemented with 10% FBS and 1% non-essential amino acids (NEEA) at 37°C and 5% CO_2.

Organoids

Forebrain organoids were derived from human iPSC colonies as described in previous publications (Qian et al., 2016, 2018). Organoids were cultured using maturation medium and grown in SpinΩ until their addition to the transwell basolateral chamber in coculture with iBMECs. The medium was changed every other day. During culture in SpinΩ, organoids were kept as 5 to 10 per well and after addition to transwell basolateral chamber, 3 to 5 organoids per well were used.

METHOD DETAILS

Differentiation of iBMECs from human pluripotent stem cells

Stem cells were thawed on Matrigel™ coated flasks and passaged once before starting the differentiation. The stem cell media (mTESR1) was changed to growth media containing knockout serum replacer to initiate differentiation as indicated in previous publications (Lippmann et al., 2012, 2014; Neal et al., 2019). After day 5, the growth media was switched to EC media supplemented with 1X B27 supplement, 20 ng/mL bFGF and 10 μM of retinoic acid (RA). After 48 h incubation at 37°C, the cell monolayer was dissociated with Accutase. Cells were seeded on Collagen IV (400 μg/mL) and Fibronectin (100 μg/mL) coated plates using supplemented EC media without RA.

Differentiation of cortical neural progenitor cells from hiPSCs

In brief, iPSC lines (C1-2 and C3-2) (Wen et al., 2014) were differentiated into forebrain-specific hNPCs using embryonic body medium and neural induction medium (NPC medium) as described previously (Tang et al., 2016; Wen et al., 2014). The hNPCs were maintained with NPC medium containing B27 supplement in Matrigel™ coated plates.

Tube formation assay

For the tube formation assay, plates were coated with 2 mg/mL of Matrigel™ using 500 μL of solution per well in a 24 well plate. Plates were incubated for 60 min at 37°C. After iBMECs differentiation, cells were detached from the culture vessel using incubation with trypsin at 37°C. After cells were in suspension, they were washed and collected in fresh EC media, then centrifuged for 5 min at 200 g. Cell pellets were resuspended in EC media containing 40 ng/mL of VEGF, 1 × 10^5 cells per well were plated and incubated at 37°C and 5% CO_2. Using a phase-contrast microscope, tube formation was assessed 12 h post seeding.

Measurement of transepithelial/endothelial electrical resistance (TEER)

STX2 electrodes attached to an EVOM Volt/Ohm meter (World Precision Instruments) were used to measure the resistance of the endothelial cell cultures in a transwell plate setup. The STX2 electrodes were placed in the transwell plate making contact between the media on the upper and the lower compartment of the plate. The resistance (Ω) values were measured 5 times in each transwell, including a cell-free control to account for the membrane's resistance. The Ω values were adjusted with the surface growth area (cm^2) of the membrane to obtain the TEER (Ω.cm^2) values of the barrier formed by the iBMECs.

Monocyte migration assay

THP-1 monocytes were used for the transmigration assays. In a transwell set up, 6 × 10^5 iBMECs were seeded on the apical side of a transwell with an 8 μm membrane pore size, no cells were seeded on the basolateral side. At 48 h post iBMECs seeding, 5 × 10^4 THP-1 cells were added to the apical side and incubated for 24 h at 37°C and 5% CO_2. After 18 h, the medium on the basolateral chamber was collected and the cells transmigrated were counted using a hemocytometer. In assays measuring the effect of chemoattractant (MCP-1 50 ng/mL), it was added to media on the basolateral chamber and TNFα (10 ng/mL) was added to the apical chamber where the iBMECs were seeded.

Sodium fluorescein assay

Media in the upper compartment of the transwell was replaced with 100 ng/mL sodium fluorescein (Na-F) solution diluted in fresh EC media. Every 30 min during the following 2-h window, 500 μL were removed from the lower compartment of each transwell while immediately replacing the taken volume with 500 μL of fresh media. 100 μL of the taken volume was aliquoted in a 96-well plate to measure the concentration of Na-F flowing through the membrane with a spectrophotometer using Ex (λ) 485 ± 10 nm and Em

(λ) 530 ± 12.5 nm. The assay was performed with technical triplicates for the fluorescence reading. The permeability coefficient value was calculated as described (Dehouck et al., 1992; Dohgu et al., 2005).

Efflux transporter assay

P-glycoprotein functionality was assessed using its preferred substrate, rhodamine 123 (Sigma). iBMEC monolayers were preincubated for 1 h at 37°C with or without 5 μM of p-glycoprotein inhibitor, cyclosporin A (Sigma). iBMECs were then incubated with rhodamine 123 (10 μM) for 1 h at 37°C with or without the inhibitor. Cells were then washed three times with ice-cold PBS and lysed with 5% Triton X-100 (TX-100; Fisher). Fluorescence (485-nm excitation and 530-nm emission) was measured using a plate reader and normalized to cell counts obtained using a hemacytometer.

SINV full-length cDNA plasmids and SVN cDNA mutant construction

SP6 transcription plasmids of SVN, SVNI, and GFP-expressing SVN mutant R47 (R47-GFP) were kind gifts from Dr. Charles M. Rice (Dubuisson et al., 1997; Frolova et al., 2002; Rice et al., 1987). All these GFP viruses included a subgenomic GFP reporter. The SVN mutants bearing nonsynonymous mutations in E2 (K190M, E260K, K190M + E260K) or 5′ UTR (U8G) were constructed on SVN or R47-GFP. Briefly, we first amplified specific E2 or 5′ UTR region with unique restriction sites flanking the mutation site from SVN. We then inserted these amplified fragments into TOPO vector to obtain E2 and 5′ UTR fragment-containing TOPO plasmids. Then we conducted mutagenesis on the TOPO plasmids with corresponding mutation primers (Table S1) by using QuikChange Lightning site-directed mutagenesis kit. The mutated E2 and 5′ UTR fragments were then digested with enzymes targeting the flanking restriction sites and ligated into SVN or SVN-GFP.

Alphavirus propagation, titration, and infection

All the SINV cDNA plasmids were first linearized with XhoI and transcribed into 5′-capped RNA transcripts with SP6 polymerase. The synthesized viral RNAs were then electroporated into BHK-21 cells (Bick et al., 2003). 400 μL of 8 × 10^6 cells were pulsed with 3 μg viral RNA in a 2mm cuvette for 5 times (1 s between pulse interval, 99μs, 960 volts). The machine model for electroporation is BTX ECM 830. The virus-containing supernatants were collected and stored at −80°C freezer 48 h post electroporation.

Virus titrations were carried out by plaque assays on BHK-21 cells. Virus stocks were sequentially 10-fold diluted in 1% FBS-containing PBS and further incubated with BHK-21 monolayers in 6-well plates for 1 h at 37°C. Virus diffusion was then confined by adding 2.25% Avicel-containing culture medium and incubated at 37°C for 24 h. Cells were fixed by 7% formaldehyde for 1 h and stained with crystal violet for 3 h.

For infection, alphaviruses were diluted in PBS with 1% FBS in minimal inoculum (200 μL per well in a 6-well plate) on top of the cells for absorption to take place. The cells were incubated at 37°C for one hour with gentle shaking every 15 min before fresh medium was added to the cells.

Flavivirus propagation and infection

To prepare the viral stocks of ZIKV, DENV and YFV, C6/36 cells were seeded in culture flasks and infected with desired viruses at multiplicity of infection (MOI) between 0.1 and 0.5. The cells were then incubated with the viral inoculum for 1 h at room temperature with gentle shaking every 15 min. Next, fresh medium was added to the culture flask and cells were incubated at 28°C and 5% CO_2 for 5–10 days. Supernatant was then collected at desired time and filtered through 0.2μm filter before aliquoting and storing at −80°C. To prepare the viral stocks of WNV, confluent monolayers of BHK-21 cells were infected at a multiplicity of infection (MOI) of 0.1 and culture fluids were harvested at 32 h post infection. Clarified culture supernatant was aliquoted and stored at −80°C. USUV and JEV were amplified once in Vero cells grown in M199 medium containing 2% FBS. Cells were infected with MOI of 0.01 and supernatants were collected at 72 h.

For infection, cells were seeded in culture vessels one day before the experiment. Desired amount of virus stock was added to the cells at the indicated MOI. The cells were incubated for 2 h at 37°C with gentle shaking every 15 min before the inoculum was removed and fresh medium was added.

Titration of flaviviruses

Focus forming assay

Titers of ZIKV, DENV or YFV samples were quantified as focus-forming units (FFUs) using Vero cells. Briefly, Vero cells were seeded on 96-well plates (2 × 10^4 cells/well) and cultured in DMEM with 10% FBS overnight at 37°C. For each viral sample, 10-fold serial dilution was performed and 100 μL of diluted sample were added to each well in triplicates after removing the culture media. Plates were incubated at 37°C for 2 h to ensure complete infection before diluted viral solution was aspirated out and replaced with 150 μL of DMEM containing 2% FBS and 1% of methyl cellulose. After 48 h (ZIKV) or 72 h (DENV and YFV) of incubation, the cells were fixed using 4% paraformaldehyde followed by 3 washes of PBS. Fixed cells were then blocked with PBTG (PBS with 0.2% Triton X-100, 1% bovine serum albumin (BSA) and 10% normal goat serum) for 1 h at room temperature and incubated with anti-flavivirus envelope 4G2 antibody (1:500 diluted in PBTG) overnight at 4°C followed by 3 washes of PBS. The cells were next incubated with goat-anti-mouse IgG horseradish peroxidase (HRP) secondary antibody for 1 h at room

temperature. After 3 washes with PBS, 50 μL of DAB substrate was added to each well and incubated for 5-10 min to allow the visualization of the foci. The foci were then counted manually and the FFU were calculated based on the results.

Plaque forming assay

Titers of the WNV samples were determined as plaque-forming units (PFU) on BHK-21 cells. Titers of USUV and JEV samples were determined as PFUs on Vero cells that cultured in M199 medium containing 2% FBS. Virus samples were serially diluted 10-fold and 100 μL of each dilution was added to duplicate wells of 6 well plates containing confluent cell monolayers. After incubation of the plates for 1 h at 37°C, the virus inoculum was removed and 2 mL of agarose overlay medium was added. The overlay media consisted of a 1:1 (vol/vol) mixture of 1% molecular biology grade agarose in water and 2X MEM that contained 2.5% FCS, 2.88% $NaHCO_3$, 2% L-glutamine, and 20 μg/mL of gentamicin. At 72 h post infection, the agarose was removed and the plaques were visualized by staining the cells with 0.05% crystal violet in 10% ethanol.

Generation of IFITM1-expressing cell lines

IFITM1 was cloned by PCR amplification using primers that contain either *BamH*I or *Eco*RI restriction site. The amplified fragments were then digested with the desired restriction enzymes and inserted into the pUltra lentiviral vector (Lou et al., 2012). For production of lentiviral particles, 293T cells were plated one day before co-transfection with IFITM1 lentiviral vector and packaging plasmids using Lipofectamine 2000 according to the manufacturer's directions. Medium was changed into fresh supplemented DMEM medium 12 h after transfection before supernatants containing lentiviral particles was collected 72 h post transfection. The supernatants were then filtered through 0.2μm filter and stored at −80°C. For transduction of SNB-19 cells to generate IFITM-expressing cell lines, SNB-19 cells were seeded at a confluency of 40%–50% before transduction with desired lentiviral particles with polybrene (5 μg/mL). 72 h post transduction, cells were used either for generating single-cell clones or subjected to flow cytometry for analysis of transduction efficiency.

CRISPR knockout of IFITM proteins

To knockout IFITM proteins in iBMECs and SerCs, the gRNAs targeting IFITM1 or IFITM123 (IFITM1 target sequence TGAT CACGGTGGACCTTGGA; IFITM123 target sequence TCTAGGGACAGGAAGATGGT) were cloned into LentiCRISPRv2 backbone (Sanjana et al., 2014) and co-transfected with packaging plasmids into 293T cells for lentiviral particles production. Supernatants containing lentiviruses were harvested 72 h post transfection and filtered through 0.2μm filters prior to storage at −80°C. For transduction of iBMECs and SerCs to generate IFITM-knockout cells, cells were seeded at a confluency of 30%–40% before transduction with the desired lentiviral particles with polybrene (5 μg/mL). Puromycin (2 μg/mL) was used for selection at 72 h post transduction.

Time-course experiment of DENV infection in IFITM1-expressing cells

SNB-19 cell lines that are expressing either empty vector or IFITM1 protein were seeded onto 6-well plates to grow overnight. The following day, the cells were incubated on ice for 10 min before inoculation with DENV at MOI of 1. The cells were left on ice for 2 h to allow virus binding before washing with PBS and shifting to 37°C to allow viral entry. Cell pallets were collected at 0 and 2 h post infection on ice and 4, 8, 12, 18 and 24 h after shifting to 37°C incubation for qRT-PCR analysis.

Cell coculture experiments

Coculture of iBMECs with CNS cells in transwells

iBMECs were seeded on collagen IV (400 μg/mL) and fibronectin (100 μg/mL) coated membranes of transwells in a seeding density of 5.3×10^5 cells/cm^2. Fresh EC medium supplemented with 1X B27 was added to the transwell as 0.5 mL in the apical chamber and 1 mL in the basolateral chamber. In astrocyte or organoid coculture experiments, the medium type on the basolateral chamber changed according to the CNS cell culture added. Seeding density for astrocytes in the basolateral chamber was 1×10^5 cells and for organoids was from 3 to 5 organoids per well in 12-well plates.

Coculture of barrier cells and cell lines

iBMECs, SerCs or RMECs were seeded under confluency on pre-coated culture plates overnight before same number of Vero or GFP-tagged Huh7.5 cells were seeded into the same well for 24 h to allow monolayer formation. After that, the cell mixture was challenged with desired viruses at desired MOIs for 48 h followed by collection for indicated analysis.

Coculture of SNB-19 cells

SNB-19 cells and IFITM1-expressing single cell clone C1-3 cells were mixed at 1:1 ratio and plated in the same well in a seeding density at 2×10^4 cells/cm^2. After the monolayer formation, the cells were exposed to the desired viruses at MOI of 1. The cells were then collected at 24 h post infection for further analysis.

Cytokine multiplex analysis

Cell supernatants from untreated astrocytes or DF19 and IMR-exposed astrocytes were collected at day 2 after transwell coculture was established. Cell supernatants were cleared of cell debris by centrifugation at low speed (200 g) for 5 min and transferred to compatible centrifuge tubes for analysis with Eve Technologies' human discovery assay: Human cytokine array/chemokine array 65-plex panel (HD65).

Immunofluorescence assay

Cells were seeded on coverslips and fixed at indicated time with 4% paraformaldehyde in PBS at room temperature for 10 min. The slides were next washed 3 times with PBS, permeabilized with PBT (PBS with 0.2% Triton X-100) for 15 min and blocked with PBTG for 1–2 h at room temperature. After that, slides were incubated with primary antibodies (diluted in PBTG) at 4°C overnight or 2 h at room temperature followed by 3 washes of PBS. The slides were next stained with desired secondary antibodies for 1 h at room temperature prior to another 3 washes of PBS. Finally, the coverslips were mounted on slides using Vectashield mounting medium with DAPI for microscopy examination.

Immunofluorescence assay for astrocytes in transwell setups

At 48 h post infection, astrocytes on coverslips from the basolateral wells of the BBB model were fixed with 4% paraformaldehyde in PBS for 10 min at room temperature, permeabilized with cold 0.1% Triton X-100 in PBS, washed with PBS, and then incubated in blocking buffer (5% horse serum in PBS) for 1 h at room temperature. Cells were incubated with primary antibodies diluted in blocking buffer at 4°C, washed 3 times with PBS at room temperature and incubated with Alexa Fluor 488, or Alexa Fluor 594/555, or Alexa Fluor 647 conjugated secondary antibody and 0.5 μg/mL of Hoechst 33,258 dye for 1.5 h. After washing with PBS to remove unbound secondary antibody, the coverslips were mounted on slides with ProLong Gold antifade mounting media. The primary antibodies used were mouse anti-dsRNA antibody and rabbit anti-S100B. Images were obtained with an Axio Observer Z1 microscope (Zeiss) using a 40× oil immersion objective.

Immunofluorescence staining of brain cerebral cortex tissue sections

Brain cerebral cortex tissue sections were first deparaffinized and rehydrated by immersing the slides through the following reagents: xylene (5 min for 3 times), 100% ethanol (10 min for twice), 95% ethanol (10 min for twice), 70% ethanol (10 min for twice), 50% ethanol (10 min for twice) and distilled water (5 min for twice). The slides were next brought to a boil in 10mM sodium citrate buffer (pH 6.0) in the microwave for antigen retrieval and kept at a sub-boiling temperature for 10 min before cooling on the bench-top for 30 min. After that, the slides were washed twice in distilled water, permeabilized with 1% normal goat serum (NGS) in PBS-T (PBS with 0.4% Triton X-100) for 10 min and blocked with 5% NGS in PBS-T for 30 min. Tissue sections were incubated with primary antibodies (diluted in 1% NGS in PBS-T) and incubated at 4°C overnight followed by 2 washes prior to incubation with secondary antibodies for 1 h at room temperature. After washing twice with 1% NGS in PBS-T, the slides were dehydrated by immersing slides through 95% ethanol, 100% ethanol and Xylene twice for 2 min each. Finally, Vectashield mounting medium with DAPI was added to the sections and the slides were topped with coverslips for microscopy examination.

Flow cytometry

Cells were washed twice with ice-cold PBS and trypsinized for collection at indicated times. Collected cell pellets were then washed once with wash buffer (1% BSA diluted in PBS) and pelleted again at 500 g for 5 min before fixing with 2% paraformaldehyde for 15 min at room temperature. After that, the samples were permeabilized with permeabilization buffer (0.2% Tween 20 in wash buffer) and incubated with anti-flavivirus envelope (4G2) antibody (1:500 diluted in permeabilization buffer) for 1 h at room temperature. After washing with wash buffer, samples were stained with secondary antibody anti-mouse Cy3 (1:500 diluted in permeabilization buffer) for 30 min at room temperature. The samples were then washed with wash buffer and resuspended in PBS for analysis by flow cytometry.

Western blotting

Samples were harvested and lysed in laemelli buffer immediately before boiling at 100°C for 15 min. Primary human BMEC lysate in a modified RIPA buffer was purchased from ScienCell Research Laboratories. Proteins in each cell lysate were separated by 12%–15% sodium dodecyl sulphate–polyacrylamide gel electrophoresis (SDS-PAGE) and transferred to 0.2 μm PVDF membranes. The membranes were next blocked in 5% milk diluted in PBST (PBS containing 0.1% Tween 20) and incubated either for 1 h at room temperature or overnight at 4°C. After that, primary antibodies were diluted in block solution and incubated with the membrane for 2 h at room temperature or overnight at 4°C. The membranes were next washed 3 times with PBST and incubated with the HRP-conjugated secondary antibodies at room temperature for 1 h before 3 washes with PBST. Finally, a chemiluminescent HRP substrate was applied to the membrane for detection of proteins.

Quantitative real-time RT-PCR

Total RNAs were extracted from harvested cell pellets using RNAeasy Plus Kit according to the manufacturer's instructions. 1μg of purified RNA were used to synthesize cDNA using Superscript III First-Strand Synthesis System with random hexamer primers. Quantitative PCR assays were performed using SYBR Green qPCR Master Mix on an ABI 7500 Fast machine with gene- or virus-specific primers. All primers are listed in Table S2. For analysis of the fold changes of mRNA expression of the desired genes, all the results were normalized to GAPDH mRNA in the control samples and calculated using the ΔΔCt method.

QUANTIFICATION AND STATISTICAL ANALYSIS

Image analyses and quantification are performed by ImageJ. Graphpad 9.0 is used for all statistical analysis. Results are shown as means ± standard deviation (SD) unless stated otherwise. Statistical significance was indicated as: ns (no significance), * ($p < 0.05$), ** ($p < 0.01$), *** ($p < 0.001$) and ****$p \leq 0.0001$ in the figures and figures legends.